



# A study of the light travel time effect in short-period MOA eclipsing binaries via eclipse timing

M. C. A. Li,<sup>1★</sup> N. J. Rattenbury,<sup>1★</sup> I. A. Bond,<sup>2</sup> T. Sumi,<sup>3</sup> D. P. Bennett,<sup>4</sup> N. Koshimoto,<sup>3</sup> F. Abe,<sup>5</sup> Y. Asakura,<sup>5</sup> R. Barry,<sup>6</sup> A. Bhattacharya,<sup>4</sup> M. Donachie,<sup>1</sup> P. Evans,<sup>1</sup> A. Fukui,<sup>7</sup> Y. Hirao,<sup>3</sup> Y. Itow,<sup>5</sup> K. Masuda,<sup>5</sup> Y. Matsubara,<sup>5</sup> Y. Muraki,<sup>5</sup> M. Nagakane,<sup>3</sup> K. Ohnishi,<sup>8</sup> To. Saito,<sup>9</sup> A. Sharan,<sup>1</sup> D. J. Sullivan,<sup>10</sup> D. Suzuki,<sup>4</sup> P. J. Tristram<sup>11</sup> and A. Yonehara<sup>12</sup>

<sup>1</sup>Department of Physics, University of Auckland, Private Bag 92019, Auckland, New Zealand

<sup>2</sup>Institute of Natural and Mathematical Sciences, Massey University, Private Bag 102-904, North Shore Mail Centre, Auckland, New Zealand

<sup>3</sup>Department of Earth and Space Science, Graduate School of Science, Osaka University, 1-1 Machikaneyama, Toyonaka, Osaka 560-0043, Japan

<sup>4</sup>Department of Physics, University of Notre Dame, Notre Dame, IN 46556, USA

<sup>5</sup>Solar–Terrestrial Environment Laboratory, Nagoya University, Nagoya 464-8601, Japan

<sup>6</sup>Astrophysics Science Division, NASA Goddard Space Flight Center, Greenbelt, MD 20771, USA

<sup>7</sup>Okayama Astrophysical Observatory, National Astronomical Observatory, 3037-5 Honjo, Kamogata, Asakuchi, Okayama 719-0232, Japan

<sup>8</sup>Nagano National College of Technology, Nagano 381-8550, Japan

<sup>9</sup>Tokyo Metropolitan College of Industrial Technology, Tokyo 116-8523, Japan

<sup>10</sup>School of Chemical and Physical Sciences, Victoria University, Wellington, New Zealand

<sup>11</sup>University of Canterbury, Mount John Observatory, PO Box 56, Lake Tekapo 8770, New Zealand

<sup>12</sup>Department of Physics, Faculty of Science, Kyoto Sangyo University, 603-8555 Kyoto, Japan

Accepted 2018 July 31. Received 2018 July 31; in original form 2018 May 3

## ABSTRACT

A sample of 542 eclipsing binaries (EBs) with periods shorter than 2 days was selected from the Microlensing Observations in Astrophysics (MOA) EB catalogue (Li et al.) for eclipse-time variation analysis. For this sample, we were able to obtain a time series from MOA-II spanning 9.5 yr. We discovered 91 EBs, out of the 542 EBs, with detected light-travel-time effect signals suggesting the presence of tertiary companions with orbiting periods from 250 d–28 yr. The frequency of EBs with tertiary companions in our sample increases as the period decreases and reaches a value of 0.65 for contact binaries with periods shorter than 0.3 d. If only those contact binaries with periods  $<0.26$  d are considered, the frequency even goes to unity. Our results suggest that contact binaries with periods close to the 0.22-d contact binary limit are commonly accompanied by relatively close tertiary companions.

**Key words:** methods: analytical – binaries: close – binaries: eclipsing.

## 1 INTRODUCTION

Microlensing is a rare astrophysical phenomenon predicted by Einstein’s general relativity (Einstein 1936). Detection of microlensing events requires the capability to monitor millions of stars simultaneously and was thought unachievable until the advent of CCD cameras and wide-field observation techniques. Because of the observational strategy, microlensing surveys would result in a large amount of photometric data of variable objects (e.g. Soszyński et al. 2016, 2017). The Microlensing Observations in Astrophysics survey (MOA-II), for instance, has collected  $\sim 100$  TB of data for millions

of variable objects in fields towards the Galactic bulge (GB) since the project began in 2006 (Sumi et al. 2013) and over 8000 eclipsing binaries (EBs) in two MOA fields were identified recently by Li et al. (2017). Amongst them, three contact binaries were further discovered to exhibit light-travel-time effect (LTTE) signals in their observed-minus-calculated (O–C) diagrams, indicating the presence of stellar tertiary companions with orbiting periods between 250 and 480 d (Li et al. 2017).

The LTTE is an effect associated with the change in orbital motion that appears in an EB with a tertiary companion, wherein the EB’s centre of mass is no longer stationary but moving around the barycentre of the whole three-body system (Borkovits et al. 2016). From an observer’s point of view, the movement of the EB’s centre of mass might be reflected by the measurement of times of eclipse

\* E-mail: mli351@aucklanduni.ac.nz (MCAL);  
n.rattenbury@auckland.ac.nz (NJR)

minima that occur later or earlier cyclically than expected, due to the finite speed of light and varying distances between the conjunction and the observer. Analysing the eclipse-time variation (ETV) via O–C diagrams, otherwise known as the ETV method, has been a traditional technique to detect LTTE in EBs, with or without spectroscopic information (Mayer 1990; Zasche et al. 2016; Zasche, Wolf & Vraštil 2017). Nevertheless, before the era of space telescope surveys, the number of EBs with detected LTTE signals was limited and triple systems found by the ETV method tended to have outer periods longer than several years or decades, because of poor precision in ground-based photometry and insufficient frequency of eclipse timings on the Earth. The majority of triple systems identified via the ETV method, unsurprisingly, come from the *Kepler* space mission (Gies et al. 2012; Borkovits et al. 2015, 2016). However, stellar triples with outer periods longer than 4 yr are obviously deficient in *Kepler* triple candidates, due to the limited duration (i.e. 1470 d) of the mission. Such a bias in the population of stellar triples identified via the ETV method may be reduced using the photometric data of long-term ground-based surveys such as MOA-II.

We are interested in searching for and investigating the population of triple systems in the MOA EB catalogue using the time series from MOA-II, which has a longer time span than the previous work of Li et al. (2017). In this article, we first review the physics of the LTTE in Section 2 and present the method of eclipse timing in Section 3. The criteria for our sample selection are presented in Section 4. The observation and data reduction processes are described briefly in Section 5. We outline the analysis work in detail in Section 6 and present the results in Section 7. We finally discuss and conclude the article in Section 8.

## 2 LIGHT TRAVEL TIME EFFECT

Changes in orbital periods were already observed in many EBs a century ago. Chandler (1888) suggested that the observed period changes in Algol resulted from the LTTE due to the presence of a tertiary object. However, it was after Woltjer (1922) was able to perform an LTTE calculation that the LTTE was seriously considered as a plausible explanation. Later, Irwin (1959) proposed an analytical model of the LTTE using the O–C diagram in terms of stellar masses and orbital parameters. As a simple tool requiring only photometric measurements, the O–C diagram has traditionally been used to detect or study physical phenomena that induce changes in the occurrence times of stellar events such as eclipses in EBs and regular pulsations in Cepheid and RR Lyrae variables, etc. For an EB, the O–C diagram represents variations in the times of its eclipse minima, which are determined by the following equation:

$$\Delta = T_o(E) - T_c(E) = T_o(E) - T_0 - P_s E, \quad (1)$$

where  $T_o(E)$  and  $T_c(E)$  denote the observed and calculated times of the  $E$ th eclipse minimum,  $T_0$  represents the reference epoch and  $P_s$  denotes the average eclipsing period. The general ETV model involving the LTTE is defined by

$$\Delta = c_0 + c_1 E + c_2 E^2 - \frac{a_{AB} \sin i_2}{c} \frac{(1 - e_2^2) \sin(v_2 + \omega_2)}{1 + e_2 \cos v_2}, \quad (2)$$

where the zeroth- and first-order coefficients,  $c_0$  and  $c_1$ , in the polynomial of  $E$  provide the corrections in  $T_0$  and  $P_s$ , respectively, while the second-order coefficient,  $c_2$ , is equal to half the rate of change in the period, regardless of its origin. The parameters in the LTTE term, i.e. the last term in equation (2), include eccentricity ( $e_2$ ), true anomaly ( $v_2$ ), argument of periastron ( $\omega_2$ ), inclination ( $i_2$ ) and the

semimajor axis of the absolute orbit,  $a_{AB}$ , equal to  $(m_C/m_{ABC})a_2$ . The period ( $P_2$ ) and the time of periastron ( $\tau_2$ ) of the tertiary object are also needed implicitly when calculating  $v_2$ . The LTTE term, therefore, depends on six parameters. Note that  $m_C$  is the tertiary object's mass,  $m_{ABC}$  the total mass of the triple system,  $a_2$  the semimajor axis of the tertiary object's orbit around the EB's centre of mass and  $c$  the speed of light. The amplitude of the LTTE is defined by

$$A_{\text{LTTE}} = \frac{a_{AB} \sin i_2}{c} \sqrt{1 - e_2^2 \cos^2 \omega_2}. \quad (3)$$

Unfortunately, the semimajor axis of the absolute orbit,  $a_{AB}$ , and the inclination,  $i_2$ , are degenerate in the LTTE model. However, the mass function,  $f(m_C)$ , defined as

$$f(m_C) = \frac{m_C^3 \sin^3 i_2}{m_{ABC}^2} = \frac{4\pi^2 a_{AB}^3 \sin^3 i_2}{G P_2^2}, \quad (4)$$

can be calculated when the LTTE solution is known. Then we can calculate the amplitude of the LTTE via the approximation equation, given by

$$A_{\text{LTTE}} \approx 1.1 \times 10^{-4} f(m_C)^{1/3} P_2^{2/3} \sqrt{1 - e_2^2 \cos^2 \omega_2}. \quad (5)$$

Note that the period and amplitude are in days and the masses are in units of  $M_\odot$ . The minimum mass of the tertiary object can also be estimated by the mass function, assuming the inner binary is of solar type, i.e.  $m_{AB} = 2 M_\odot$ . From equation (5), we know that the LTTE amplitude decreases as the outer period decreases. Because of this, and owing to insufficient precision in ground-based photometry and difficulty in performing eclipse timing frequently enough on Earth to cover a short-period LTTE cycle satisfactorily, LTTEs associated with triple systems with outer periods shorter than two years were rarely detected by ground-based telescopes and stellar triples identified on Earth tend to be those with tertiary periods longer than several years or even decades.

Additional dynamical perturbations may dominate over perturbations due to LTTE and become observable in an O–C diagram, if the tertiary companion interacts tightly with the inner binary in a triple system (Borkovits et al. 2016). In the case of the inner binary being eccentric, the ETV term corresponding to apsidal motion may have to be included as well. The apsidal motion may be regarded simply as linear variation in  $\omega_1$ , as a result of the apsidal line of the inner binary's orbit rotating with a constant angular velocity in the direction of the orbital motion arising from the tidal deformation of the shapes of the binary components or relativistic effects (Cowling 1938; Sterne 1939; Borkovits et al. 2015). Nonetheless, the presence of a tertiary companion may induce the apsidal motion of the inner binary to behave in a complicated manner in which no orbital parameters, except the semimajor axes, would remain constant (Naoz et al. 2013; Borkovits et al. 2015 and further references therein). Since we restricted our study to short-period binaries for which circular orbits should be established, we thus assumed apsidal motions were negligible.

Although the detection of a LTTE signal with multiple cycles is strong evidence for the existence of a tertiary companion in an EB, several mechanisms, such as mass transfer between the EB's components, magnetic braking and the Applegate effect (Applegate 1992), can produce quadratic variation in the orbital period that may be confused with a LTTE cycle of period longer than the data time span. Star spots can also produce spurious ETVs that mimic LTTE behaviour (Tran et al. 2013). In order to justify the plausibility of a LTTE solution to the ETV curve, Frieboes-Conde & Herczeg (1973) suggested four general criteria: (1) the shape of the ETV

curve must follow the analytical form of a LTTE solution; (2) the ETVs of the primary and secondary eclipses must be consistent with each other in both phase and amplitude; (3) the estimated mass or lower limit to the mass of the tertiary companion derived from the mass function must be in accord with the photometric measurements or the limit on the third light in the system; (4) the variation in the system's radial velocity must be in accord with the LTTE solution. Obviously, without radial velocity data, criterion (4) could not be satisfied. In addition to these criteria, we also employ the Bayesian information criterion (BIC) as an extra criterion:

$$\text{BIC} = n \ln \left( \frac{1}{n} \sum_i (x_i - \hat{x}_i)^2 \right) + k \ln n, \quad (6)$$

where  $x_i$  are the measurement values,  $\hat{x}_i$  are the calculated values from the model fit,  $n$  is the number of measurement points and  $k$  is the number of variable parameters in the model fit. The goodness of the BIC as a model selection criterion is that it includes the penalty term, i.e.  $k \ln n$ , to disfavour the case of overfitting by adding parameters. We shall accept detected LTTE signals as genuine if they satisfy the first and second criteria, as well as the fits associated with the LTTE signals having lower values of the BIC compared with the quadratic fits associated with the ETV produced by other mechanisms.

### 3 ECLIPSE TIMING METHODS

The orbital motion of an EB, if it is purely a two-body system, should be described and predicted exactly by Kepler's equation as long as apsidal motion is not involved. Thus, EBs can be used as precise clocks in astronomy. However, accurate eclipse timing is challenging on the Earth. Individual eclipses usually last a few hours. Ground-based observation often fails to obtain complete coverage of an eclipse, because of the poor condition of the night sky. Traditionally, the time of an eclipse minimum would be derived using the Kwee–van Woerden method (Kwee & van Woerden 1956). Several recent studies to look for circumbinary planets in post-common-envelope binaries applied this method to derive the times of eclipse minima (e.g. Lee et al. 2014; Baran et al. 2015). The Kwee–van Woerden method, however, cannot work properly if an eclipse is not symmetric about its minimum, the distribution of data points over the eclipse is not even (i.e. observations over the eclipse were not taken in regular cadences) or the number of data points covering the eclipse is too low. The Kwee–van Woerden method also, as mentioned in Pribulla et al. (2012), usually underestimates the uncertainties in the derived times. The eclipse template method, as far as we know, has turned out to be an alternative method that is commonly used nowadays. Various ways to create an eclipse template were proposed and used by different research groups. A high-order polynomial fit (`polyfit`) was used by the *Kepler* group in order to create an approximate eclipse template. A realistic eclipse template might be derived by fitting the photometric light curve using an EB modelling package such as PHOEBE (Prša et al. 2016).

The template generation methods mentioned so far are, however, either impracticable or unsatisfactory for our study. Although the template of a grazing eclipse can be generated appropriately by a quartic polynomial using the `polyfit` code, we found that it has trouble producing an appropriate template for a total eclipse. A higher-order polynomial might be adopted to generate templates for total eclipses, but it often yielded templates with rippling bottoms and the minima did not correspond appropriately to the eclipse minima. We desired a template generation method that was workable for grazing and total eclipses. For these reasons, we finally decided

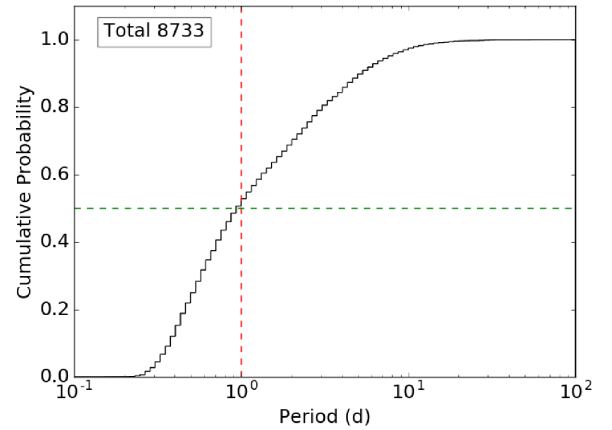


**Figure 1.** Cumulative distribution of period for 8733 EB candidates identified in the work of Li et al. (2017). The black curve shows the cumulative distribution of period from 0.1 d to 100 d for all MOA EBs identified in the GB9 and GB10 fields. The horizontal dashed line (green) marks a level of cumulative probability equal to 0.5, while the vertical dashed line (red) marks a period of 1 d.

to adopt the phenomenological light-curve model of EBs proposed by Mikulášek (2015). Considering only the portion of an EB's light curve belonging to either the primary or secondary eclipse, the model is reduced to the function of five parameters, defined by

$$f(t_i, \theta) = \alpha_0 + \alpha_1 \psi(t_i, t_0, d, \Gamma), \quad (7)$$

where  $\alpha_0$  is the magnitude zero-point shift (i.e. the relative flux baseline level in our study) and  $\alpha_1 < 0$  is a negative multiplication constant of the eclipse profile function, i.e.

$$\psi(t_i, t_0, d, \Gamma) = 1 - \left\{ 1 - \exp \left[ 1 - \cosh \left( \frac{t_i - t_0}{d} \right) \right] \right\}^\Gamma. \quad (8)$$

Note that  $t_0$  is the time of minimum of an eclipse,  $d > 0$  is the minimum width and  $\Gamma > 0$  is the parameter specifying the pointedness of the minimum, such that  $\Gamma > 1$  corresponds to the flat minimum associated with a total eclipse. The procedures for timing eclipse minima and measuring ETVs are presented in detail in Section 6.2.

### 4 SAMPLE SELECTION

MOA-II has adopted an observational strategy in which most of its time in the sky is dedicated to routinely monitoring the same fields towards the GB every clear night with high cadences. This gives MOA-II an advantage over other microlensing surveys in obtaining eclipse time measurements from short-period EBs that would be frequent enough to reveal any short-period ETV. From the preliminary investigation of Li et al. (2017), we know that there are typically  $\sim 100$  eclipse time measurement points for MOA EBs of periods shorter than a day, while this number declines to  $\sim 19$  for MOA EBs of periods between 2 and 10 d. This implies that the MOA data should be useful for stellar companion detection and study of the frequency of tertiary companions in contact or semi-detached binaries. The detection of EBs in the MOA data base was also strongly biased towards EBs of periods  $< 1$  d. About 50 per cent of MOA EBs have periods  $< 1$  d (see Fig. 1). Interestingly, almost all MOA EBs of periods  $< 1$  d are contact binaries. This implies that the search for tertiary companions in MOA EBs of periods  $< 1$  d is equivalent to studying the frequency of contact binaries with tertiary companions. As we are concerned with the homogeneity of the sample, we focused on studying MOA EBs with periods

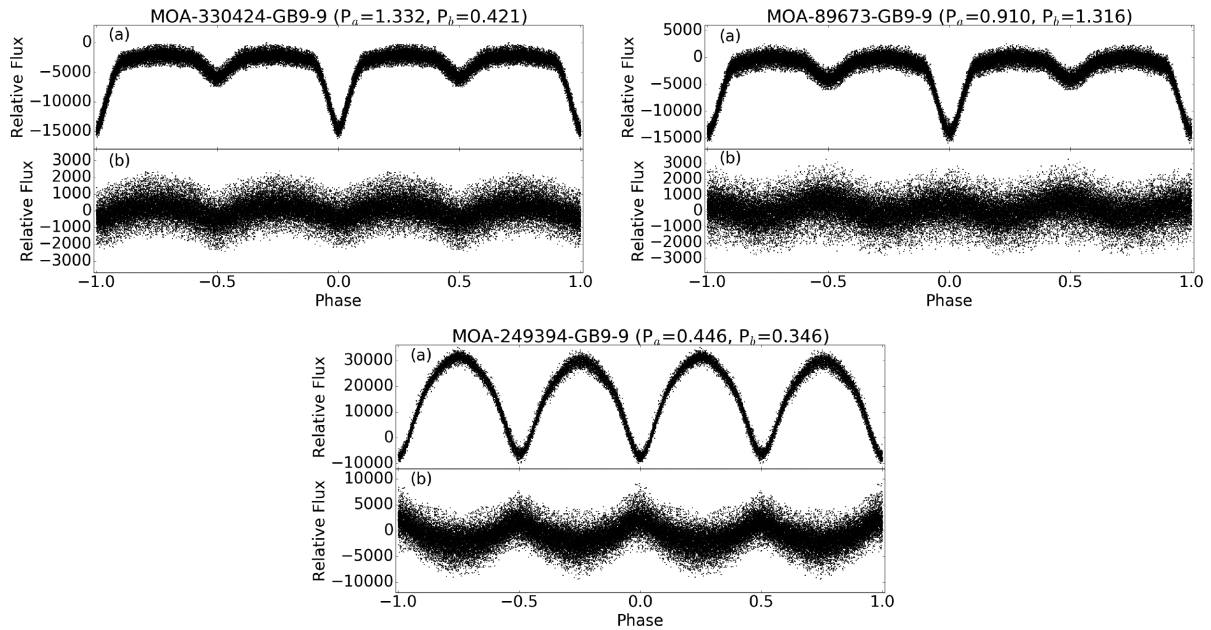


**Figure 2.** Folded light curves of the three EBs in our MOA samples from the GB9-9 and GB10-1 fields, which were discovered to have additional regular periodic signals under their main eclipsing signals. (a) The main eclipsing signals. (b) The additional periodic signals. The secondary periodic signals in MOA-330424-GB9-9 and MOA-89673-GB9-9 are the eclipsing and ellipsoidal variation curves, respectively, likely associated with EBs near them. However, the source of the secondary periodic signal in MOA-249394-GB9-9 is uncertain. We suspect that it might be an artefact from imperfect image subtraction in difference image analysis, owing to a bright variable star close to the EB in the images.

$< 2$  d and attempted to obtain the full time series of MOA EBs within this period range. There are over 4000 EBs in the MOA EB catalogue that have periods shorter than 2 d. However, generating light curves from the full MOA data base is expensive in terms of computational time and data storage space. Therefore, we restricted our study further to two subfields, GB9-9 and GB10-1, from which the full light curves could be generated easily. 542 EBs from the GB9-9 and GB10-1 fields fell into the period range between 0.22 and 2 d and no EB from these two subfields is of period  $< 0.22$  d.

## 5 OBSERVATIONS AND DATA REDUCTION

The MOA project is a Japan and New Zealand collaboration, which began in 1995; the second stage of the project started in 2006 with a 1.8-m telescope located at the University of Canterbury Mount John Observatory, New Zealand. The MOA-II telescope is equipped with the MOA-cam3 wide-field camera, which consists of  $10\,2\,k \times 4\,k$  pixel CCDs with  $15\text{-}\mu\text{m}$  pixels and provides a field of view (FOV) of  $2.18\text{ deg}^2$ , given a pixel scale of  $0.58\text{ arcsec pixel}^{-1}$ . The primary mission of the MOA project is always hunting exoplanets via microlensing. For this purpose, it has adopted a special observational strategy, in which telescope times are spent mainly on a survey towards 22 fixed fields of the GB. Images of these 22 fields were taken with cadences between 10 min and 1 h through the custom MOA-Red wide-band filter, which spans from 600–900 nm. In each field, there are 10 subfields corresponding to 10 CCD chips.

The data sets we obtained from the GB9-9 and G10-1 fields span 9.5 yr and were collected from February–November every year since 2006. Image reduction was performed following the same procedures described in Li et al. (2017), using the difference imaging analysis (DIA) method (Bond et al. 2001). The density of the light curves from the GB9-9 field is approximately uniform, while the density of the light curves from the GB10-1 field is low during the first two years, although big gaps exist, as expected, due

to the off-season periods. The exposure time of 60 s was taken for both fields over the entire observational time span. The observation time was recorded in Julian Days and calculated to be midway between the start and end times of an exposure.

## 6 ANALYSIS

### 6.1 Period analysis

In the beginning, all the light curves of our EB samples were cleaned following the light-curve procedure as in Li et al. (2017). In a nutshell, we discarded outliers that are  $4.0\sigma$  above or  $9.0\sigma$  below the relative flux mean, as well as detrending the light curves via linear regression. This cleaning procedure was iterated twice before going into the light-curve analysis. Meanwhile, we corrected the times from Julian Days (JD) to Barycentric Julian Days (BJD). Despite the time span of over 9 yr, we did not divide the light curves into segments with shorter time spans in general, except for several cases for which careful treatments in eclipse-time measurement were needed (see Section 6.2).

Since the MOA fields towards which our EBs are located are densely populated, blending with nearby stars might be present. On the other hand, stellar pulsations might be present in our EBs; in particular, a component being Cepheid or RR Lyrae, which would pulsate regularly with a period comparable to the eclipse duration, will distort an eclipse shape, causing the measurement of the time of eclipse minimum to be inaccurate. Because of these problems, we attempted first to search for an additional eclipsing or hidden pulsation signal under the main eclipsing signal. To do so, we first determined the average eclipsing period with which the 9.5-yr light curve could be properly folded using conditional entropy with trial periods  $P'_s \pm 0.01$ , where  $P'_s$  is the average eclipsing period over two MOA observational seasons provided in the MOA EB catalogue. Once the new average eclipsing period was determined and after



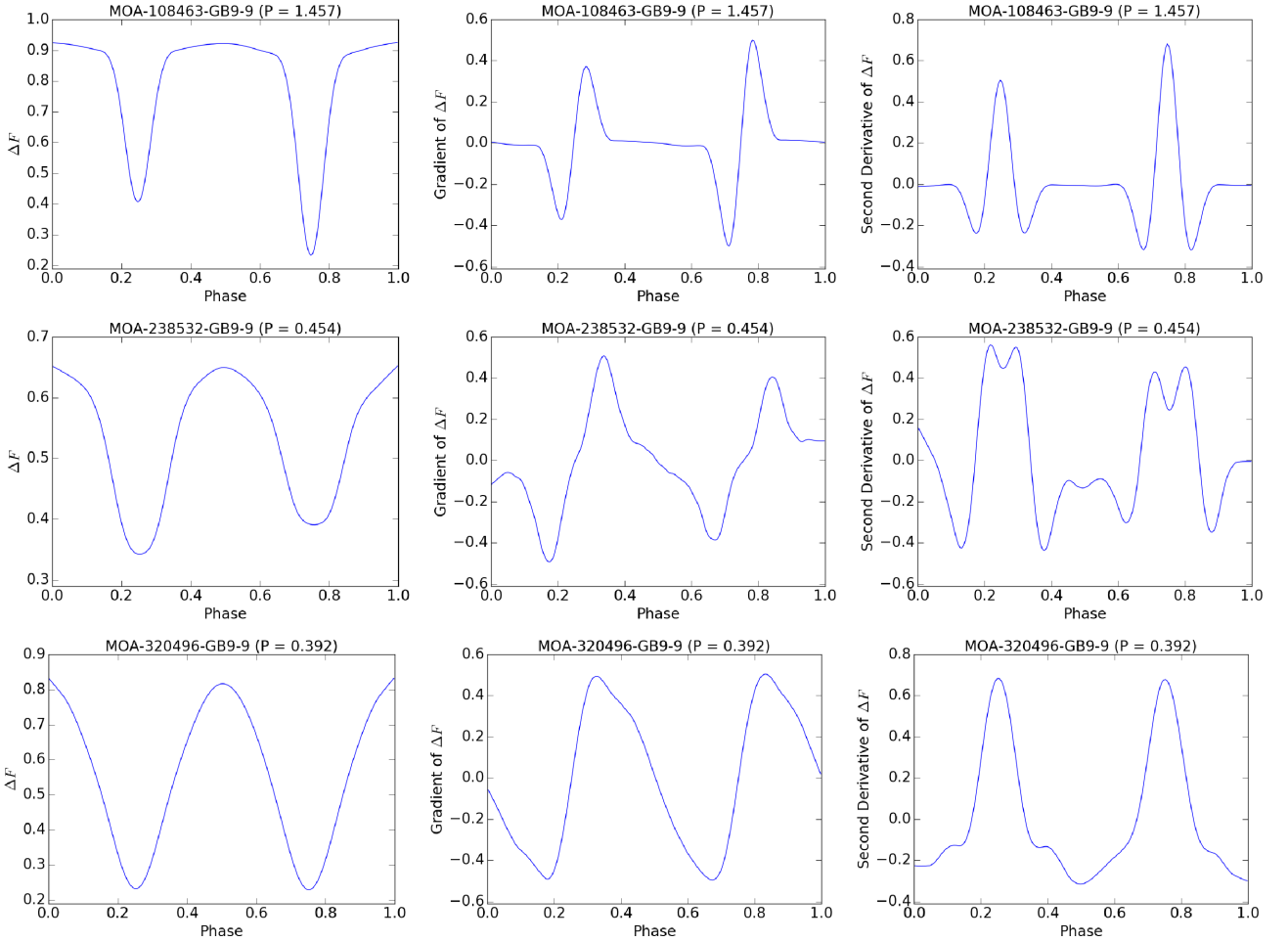


**Figure 3.** Mean light curves (left), first derivative curves (middle) and second derivative curves (right) of three representative MOA EBs. The points of ingress and egress of an eclipse are determined by calculating a pair of minima in the second derivative curve that can define the boundaries of the eclipse well, i.e. the pair of minima of the Mexican hat feature in the second derivative curve. In a few cases, no pair of minima in the second derivative curves corresponding to the ingress and egress of their primary or secondary eclipses could be derived and we used the maxima and minima in the first derivative curves to define the eclipse regions; for example, in the case of MOA-320496-GB9-9, we could not derive a pair of minima in the second derivative curve that could be used to define the boundaries of the primary eclipse, and thus the phases of the maximum and minimum in the first derivative curve were used to represent the primary eclipse’s boundaries.

checking the resultant folded light curve by eye to see if it was folded properly, we binned the folded light curve in 200 bins and created an approximate curve by calculating the mean flux value in each bin. We then produced the residual curve by subtracting the approximate curve from the folded light curve and unfolding it afterwards. The residual curve was then put through period analysis by the condition entropy algorithm, with trial periods ranging from 0.05–600 d. The residual curve folded with the output period was inspected by eye afterwards.

In this manner, we discovered three residual light curves that exhibited periodic signals. Fig. 2 shows the main eclipsing and additional periodic signals of these three EBs. The additional periodic signals in MOA-330424-GB9-9 and MOA-89673-GB9-9 are obviously associated with an EB with a period of 0.421 d and an ellipsoidal binary with a period of 1.316 d, respectively, while we suspect that the additional periodic signal in MOA-249394-GB9-9 was an artefact due to contamination by a nearby pulsating bright star or a bright EB that caused imperfect image subtraction in the DIA. The additional signals detected were subtracted from the original light curves and the average eclipsing periods were recalculated after subtraction.

## 6.2 Eclipse time measurement

To measure the times of eclipse minima, the template method using Mikulášek (2015)’s model to generate the eclipse templates was applied. The corresponding eclipse regions were determined by calculating the pairs of minima of the second derivative of the folded light curve, which corresponds to the ingress and egress phases of the eclipses. If no valid minima were obtained from the second derivative curve, we took the pair of minima of the first derivative curve between which the eclipse minimum is located as the boundaries of the eclipse region. The procedures for identifying the ingress and egress of an eclipse are as follows.

- (i) Derive the mean light curve by binning the folded light curve into 20 bins and calculating the mean flux in each bin.
- (ii) Derive the first derivative curve by calculating the gradient of the mean light curve using the function `gradient()` in `numpy`.
- (iii) Derive the second derivative curve by calculating the gradient of the first derivative curve using the function `gradient()` in `numpy`.

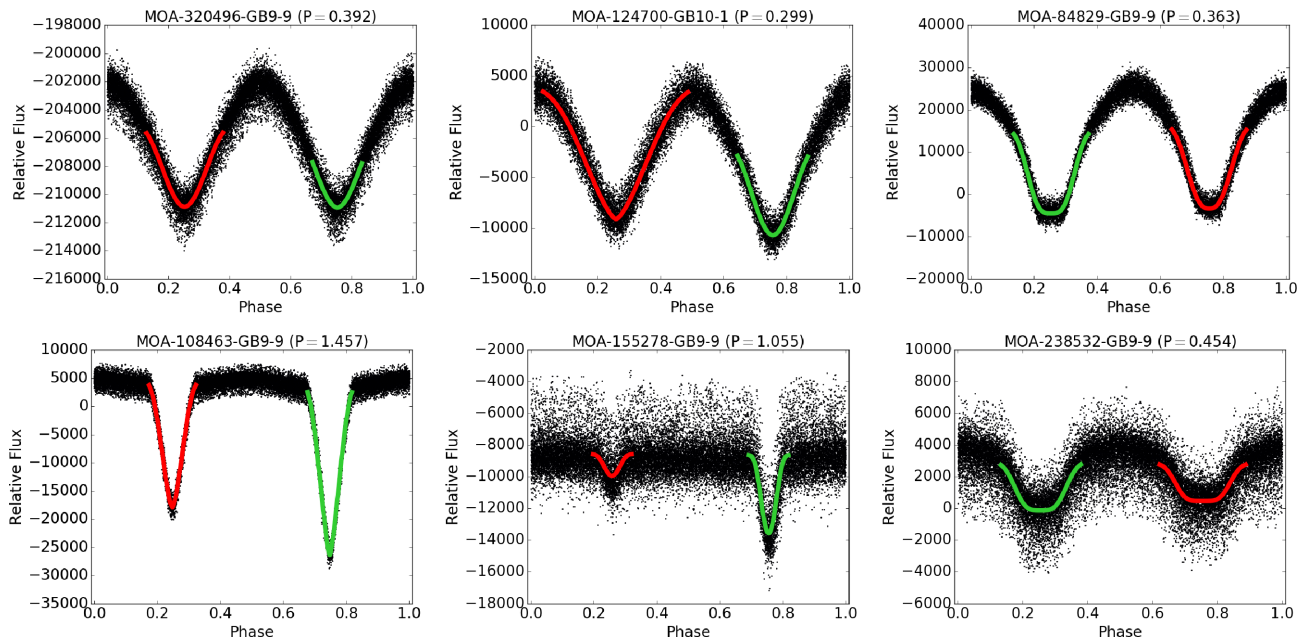


**Figure 4.** Templates of representative MOA EB light curves. The green and red curves represent the templates for primary and secondary eclipses, respectively. The templates were generated by fitting equation (7) to the eclipse regions of the folded light curves.

(iv) Smooth the curves in each step above using the method of locally weighted scatter-plot smoothing (LOWESS) provided in `statsmodels`, a Python module in statistics, and calculate the phases of maximum and minimum points using the function `argrelextrem()` in `scipy`.

(v) Take the pair of minimum points in the second derivative curve that contain the eclipse minimum as the points corresponding to ingress and egress of the eclipse.

To illustrate the situations for different types of EB light curve, we take MOA-108463-GB9-9, MOA-238532-GB9-9 and MOA-320496-GB9-9 as examples. Their mean light curves and first and second derivative curves are shown in Fig. 3. MOA-108463-GB9-9 is an Algol-type EB, as the turning points in its mean light curve corresponding to the ingress and egress of both eclipses can be easily recognized by eye. Its first derivative curve resembles an electrocardiogram, while its second derivative curve contains two Mexican hat features associated with the primary and secondary eclipses. In the case of MOA-238532-GB9-9, instead of yielding typical Mexican hat features, which have single peaks at the middles for both eclipses in the second derivative curve, double peaks were produced, indicating the presence of four contact points, which would be present for total eclipsing, in both eclipses. Unsurprisingly, the points of ingress and egress of the eclipses can be easily determined by calculating pairs of minima in the second derivative curves between which the minima of their eclipses lie accordingly. In the case of MOA-320496-GB9-9 (which seems to be a W UMa binary), we can see that its second derivative curve fails to yield a proper Mexican hat feature for the primary eclipse, having only a single minimum instead of a pair of minima that would allow us to determine the ingress and egress of the eclipse. Therefore, we instead took the phases of the maximum and minimum in the first

derivative curve as the boundary points of the region of the primary eclipse.<sup>1</sup>

Once the boundaries of the eclipse region were determined, the best-fitting template was derived by fitting Mikulášek's model, i.e. equation (7), to the portion of the folded light curve between the boundaries using `emcee`, a Python implementation of the affine-invariant ensemble sampler for Markov chain Monte Carlo (MCMC: Foreman-Mackey et al. 2013). The reference epoch,  $T_0$  in equation (1), in regard to the derived template was thus defined accordingly as  $T_0 = \phi_0 P_s + \tau_0$ , where  $\phi_0$  is the phase of the template minimum with respect to the time zero,  $\tau_0$ , which we set to be  $\tau_0 < t_{\text{obs}}$ , where  $t_{\text{obs}}$  is an observation time such that both primary and secondary eclipses are not cut in phase when we folded the light curve with respect to  $\tau_0$ . The best-fitting templates of six EBs in our MOA samples are shown in Fig. 4 as examples to demonstrate the usefulness of our template-generating method for different shapes of eclipse. Although we adopted Mikulášek's model, i.e. equation (7) is supposed to work for eclipse portions of detached EB light curves, it still generated templates that represent eclipses of contact binaries well in practice, even if the eclipse boundaries derived by our algorithm turned out to be located at or close to the maxima of the light curves, as verified by the case of MOA-124700-GB10-1 (see Fig. 4). Once the template was generated, we unfolded the light curve and then fitted each eclipse that had at least four data points across the eclipse minimum with the template. The general idea

<sup>1</sup>In our sample of 542 MOA EBs, there were only a few cases in which we failed to find the ingress and egress of eclipses from the second derivative curves and they all seemed to be either W UMa EBs or ellipsoidal binaries, after inspecting their folded light curves by eye. For them, it might be more appropriate to use the light-curve maxima to define the boundaries of their eclipse regions. Nevertheless, we did not find that it would impact the accuracy of our eclipse timing significantly.

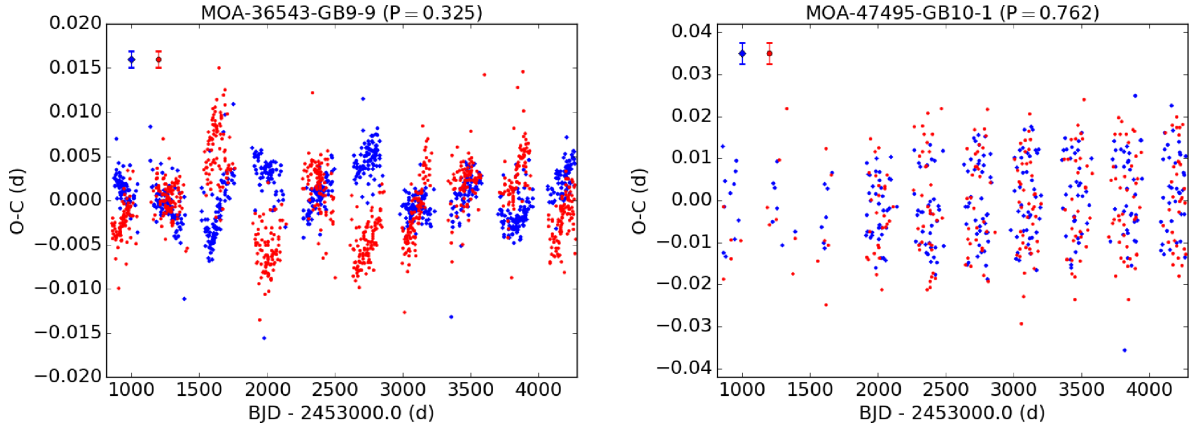


**Figure 5.** Examples of the O–C diagrams of the MOA EBs with spurious ETVs. Left: the O–C diagram of MOA-36543-GB9-9, in which the ETV curves for the primary and secondary eclipses vary cyclically and are anti-correlated to each other. Right: the O–C diagram of MOA-47495-GB10-1, which appears to have two separate curves or rapidly oscillating ETVs. The blue (diamond) points are the ETV measurements of the primary eclipses and the red (circle) points are those of the secondary eclipses. The average uncertainties for the primary and secondary eclipses are represented by the red and blue error bars, respectively, at the top-left corner of each figure. Note that the periods are in days.

**Table 1.** Boundaries of the parameters of the ETV model equation (2). Note that d denotes days, d/c days per cycle and au astronomical units.

Parameter (unit)	Lower	Upper
$c_0$ (d)	−0.1	0.1
$c_1$ (d)	−0.1	0.1
$c_2$ (d/c)	−0.1	0.1
$\log(P_2)$ (d)	$\log(P_2/2)$	$\log(2P_2)$
$e_2$	0	0.999
$\omega_2$	0	$2\pi$
$\tau_2$	0	1
$a_{AB}$ (au)	0	100

of the template method is to obtain the time of the eclipse minimum by shifting the template horizontally until the template fits the eclipse best. In reality, however, the brightness of a star may vary over time, and hence the template parameters  $t_0$  as well as  $\alpha_0$  and  $\alpha_1$  were required to vary to search for the best fit. Again, the best-fitting parameter search was executed using *emcee*. As a result, the time of the eclipse minimum was determined by the median of the projected posterior on  $t_0$ . The uncertainty in  $t_0$  was taken as the  $1\sigma$  confidence interval from the median.

The eclipse timing process described in the previous paragraph worked properly for most of the MOA EBs we studied. There are, however, six MOA EBs for which we could never derive periods with which they could be folded satisfactorily. Such a problem indicated that these EBs suffered significant ETVs. As improper folding could induce significant errors in the derived eclipse templates, we thus divided each of these EB light curves into three segments, of which the first two segments span the first seven years evenly and the third segment spans the last 2.5 yr. We then calculated the average eclipsing period for each segment and generated the corresponding templates and performed the eclipse time measurement following the same process as mentioned in the previous paragraph.

We ignored measurement points with very large uncertainties and inspected the resultant ETV curves afterwards. As expected, the ETV curves of shorter period EBs are generally denser than those of longer period EBs, given that there were more eclipsing cycles for the shorter period EBs. Cyclic or quasi-cyclic variations on a time-scale shorter than two MOA observation seasons ( $\approx 2$  yr)

were noticeable in the O–C diagrams of several samples. A few of them exhibit quasi-periodic ETVs for their primary and secondary eclipses that are highly anti-correlated: for example, MOA-36543-GB9-9 (see Fig. 5). Such anti-correlated ETVs were supposed to be due to the presence of active star spots (Tran et al. 2013). Scattering of the ETV points comparable to the average error bars on a time-scale of one MOA observational season was common in the O–C diagrams of our sample. In some cases, the ETV points dispersed such that the O–C diagrams seemed to have two separate curves or to exhibit very rapid oscillations on very short time-scales ( $< 100$  d), e.g. MOA-47495-GB10-1 (see Fig. 5). Orbital perturbations due to very short period tertiary companions could produce oscillating ETVs, which have been observed in the *Kepler* triples (Borkovits et al. 2016). However, we also suspect that this kind of ETV might be spurious, arising from stellar oscillations or pulsations (Borkovits et al. 2014). Given the frequency of and accuracy in eclipse timing from the MOA data, the proper coverage of an ETV cycle shorter than 200 d was expected to be unachievable. In order to avoid false detection of short-period LTTE cycles due to overfitting scattering of ETV points or possible spurious ETVs, we restricted the search to those LTTE cycles that have periods longer than 200 d. We also ignored the EBs in the sample with highly anti-correlated ETV cycles without any evident long-term variation for the LTTE analysis. Further discussion about this issue is presented in Section 7.

### 6.3 LTTE analysis

The O–C diagram of each EB was constructed according to equation (1), with  $P_i$  being the average eclipsing period over the full data time span and  $T_0$  being the time of the eclipse template minima, except for the six special EBs mentioned in Section 6.2, for which the average eclipsing periods and times of eclipse template minima associated with the segments of the first 3.5 yr were used instead. After a preliminary inspection, we decided to discard ETV measurement points with uncertainties  $> 0.01$  d (except for MOA-222739-GB9-9, for which we accepted ETV measurement points with uncertainties up to 0.02 d instead). Then we fitted the LTTE model, including or excluding the quadratic term of  $E$ , to the primary and secondary ETV curves simultaneously, using *pymc* (Barentsen et al. 2013),

**Table 2.** Orbital elements from the LTTE solutions for 65 EBs in the GB9-9 field. Note that  $P_1$  is the period of the inner binary determined by the conditional entropy method plus the correction,  $c_1$ , given by the best fit of equation (2) to the ETV curve and  $\Delta P_1 = 2c_2$ , where  $c_2$  is the second-order coefficient in equation (2), is the change in inner binary orbital period per orbital cycle in units of [day cycle $^{-1}$ ] and  $m_{AB}$  was taken as  $2 M_\odot$  when calculating  $(m_C)_{\min}$ .

No.	$P_1$ (d)	$\frac{\Delta P_1}{10^{-10}}$ $\times (\text{d cycle}^{-1})$	$P_2$ (d)	$e_2$	$\omega_2$ (deg)	$\tau_2$ (MJD)	$a_{AB} \sin i_2$ au	$f(m_C)$	$(m_C)_{\min}$ $M_\odot$	$\Delta BIC$
349130	0.2528512(2)	—	7926(80)	0.29(1)	1(1)	53979.7(2)	7.5(1)	0.89(4)	2.7	178.07
284305	0.5086635(1)	—	3428(96)	0.96(4)	88(5)	54621.65(4)	1.61(6)	0.048(6)	0.7	912.89
155278	1.0545500(2)	—	1888(29)	0.7(1)	35(10)	54789.43(6)	1.1(1)	0.05(2)	0.7	3.35
145571	1.2480074(6)	—	3166(84)	0.51(2)	83(5)	56119.25(4)	2.60(7)	0.23(2)	1.39	54.25
108463	1.45689719(6)	—	2374(21)	0.99(1)	200(8)	55636.74(1)	2.1(8)	0.2(3)	1.38	200.73
19030	1.1797806(3)	—	2590(115)	0.3(1)	309(28)	56176.1(1)	0.61(6)	0.004(1)	0.29	4.43
84829	0.3634425(5)	—	6136(1911)	0.41(9)	312(11)	55152.6(4)	1.1(4)	0.004(5)	0.28	900.73
351777	0.339333891(4)	—	2898(11)	0.130(9)	4(4)	54712.16(3)	0.478(2)	0.00174(3)	0.2	92.92
182318	0.39390818(1)	—	3004(25)	0.47(3)	4(3)	54285.03(4)	0.327(6)	0.00052(3)	0.13	387.54
227115	0.86548591(6)	—	2374(20)	0.98(2)	144(14)	54869.39(3)	0.8(3)	0.01(1)	0.41	9.28
217605	0.7081659(3)	−15(1)	1617(10)	0.30(4)	142(7)	54907.54(3)	1.36(3)	0.130(9)	1.07	461.82
360672	0.35884830(2)	−2.97(3)	948(1)	0.60(2)	105(2)	53915.18(4)	0.327(3)	0.0052(2)	0.3	984.98
34057	1.1061859(2)	—	2752(21)	0.99(1)	320(14)	54349.35(1)	2.1(7)	0.2(2)	1.21	13.51
72704	0.97866744(4)	—	1396(5)	0.51(3)	115(5)	55016.74(2)	0.68(2)	0.022(1)	0.52	36.79
17921	0.44477494(3)	—	2720(169)	0.5(1)	320(12)	55506.97(10)	0.19(2)	0.00011(4)	0.08	87.01
356144	0.7865492(2)	—	4424(84)	0.70(4)	6(3)	54208.43(5)	1.59(5)	0.027(3)	0.56	209.79
250567	0.34603681(2)	−2.01(4)	2498(8)	0.89(2)	173(2)	54258.05(2)	0.26(2)	0.00039(10)	0.12	380.84
157806	0.5361466(6)	—	3481(736)	0.21(7)	282(30)	56603.5(3)	0.4(2)	0.0008(10)	0.15	105.52
67484	0.24226037(8)	−2.0(1)	3021(760)	0.74(8)	193(5)	56378.7(3)	0.34(9)	0.0006(6)	0.14	110.26
182430	0.35978161(1)	—	2714(26)	0.58(5)	172(2)	53826(1)	0.37(2)	0.0009(2)	0.16	105.52
187318	0.43288552(6)	5.1(1)	844(2)	0.37(3)	236(10)	54146.46(7)	0.335(7)	0.0071(5)	0.34	759.87
220479	0.4423801(1)	—	6326(587)	0.70(4)	3(3)	54182.0(1)	1.09(8)	0.004(1)	0.28	143.13
249030	0.69573952(10)	—	2793(62)	0.77(4)	288(3)	55382.11(3)	1.87(5)	0.112(9)	1.0	240.62
155668	0.2972139(1)	−1.7(2)	1687(43)	0.8(1)	177(8)	54362.5(1)	0.4(2)	0.004(5)	0.26	51.5
109391	0.30558171(3)	—	3074(141)	0.30(6)	277(16)	55169.33(8)	0.40(2)	0.0009(1)	0.16	250.23
380523	0.34710273(8)	−2.9(2)	1325(9)	0.96(5)	100(17)	54328.05(3)	0.43(5)	0.006(2)	0.32	88.28
65718	0.3320172(1)	—	8436(562)	0.64(4)	36(4)	55843.9(1)	1.27(9)	0.0038(9)	0.27	138.62
22226	0.3603168(1)	−4.4(3)	2460(29)	0.95(5)	354(4)	54028.1(1)	0.8(4)	0.01(2)	0.39	154.63
361861	0.2794994(1)	—	7617(1234)	0.78(3)	148(4)	54606.1(2)	0.9(1)	0.0017(9)	0.2	72.07
256806	0.2665336(3)	—	10918(4822)	0.69(9)	179(8)	54488.1(6)	1.6(6)	0.005(7)	0.29	10.47
303209	0.28954488(7)	—	3687(127)	0.37(4)	163(5)	57488.72(4)	0.69(5)	0.0033(7)	0.26	57.64
159607	0.31115756(7)	5.7(1)	1247(4)	0.78(2)	329(2)	54001.20(4)	1.13(5)	0.12(2)	1.05	654.83
322149	0.4825322(2)	—	4788(200)	0.57(3)	83(4)	56622.07(6)	1.41(8)	0.016(3)	0.46	278.28
238532	0.45366092(7)	—	1093(5)	0.81(9)	137(7)	54569.77(2)	1.4(2)	0.3(2)	1.6	83.34
67250	0.4252117(1)	—	8609(1761)	0.65(7)	291(9)	55993.2(3)	0.9(1)	0.0014(8)	0.19	45.69
135452	0.5006658(9)	—	7711(2664)	0.69(9)	335(5)	55539.7(5)	2.6(8)	0.04(4)	0.65	238.14
101545	0.26379918(4)	—	1859(39)	0.6(1)	28(14)	54933.39(9)	0.69(9)	0.013(5)	0.42	209.86
83874	0.3484025(3)	—	7974(3098)	0.7(1)	146(11)	55161.9(5)	0.9(3)	0.002(2)	0.2	42.38
7772	0.31983968(5)	—	1967(252)	0.8(2)	110(45)	53972.2(7)	0.21(5)	0.0003(2)	0.11	0.05
315321	0.4189762(1)	—	3324(465)	0.8(1)	134(17)	55793.6(2)	1.0(3)	0.011(10)	0.4	32.31
367657	0.4167100(1)	2.4(4)	1373(12)	0.76(8)	152(6)	55080.16(2)	0.8(1)	0.03(1)	0.61	225.18
306577	0.448403(1)	—	4623(1106)	0.75(9)	121(11)	53919.0(7)	1.9(6)	0.05(5)	0.69	18.2
180438	0.23953468(5)	—	3569(297)	0.6(1)	170(11)	56479.3(1)	0.69(8)	0.004(1)	0.26	33.66
43392	0.7782322(2)	—	2350(39)	0.25(9)	8(9)	54525.98(9)	1.14(4)	0.036(4)	0.63	167.38
357126	0.4173683(1)	—	2329(68)	0.8(2)	276(16)	56126.51(3)	0.9(1)	0.019(9)	0.49	26.68
157098	0.4248364(1)	−7.6(3)	1355(12)	0.8(2)	55(12)	53863.2(5)	0.38(8)	0.004(3)	0.27	17.21
372358	0.43437314(9)	—	2049(54)	0.7(1)	344(9)	55682.72(5)	1.1(2)	0.04(2)	0.68	228.98
146280	0.4860822(4)	—	2773(159)	0.4(2)	155(29)	54747.1(2)	1.7(3)	0.09(4)	0.92	18.23
333535	0.7721721(1)	—	2940(242)	0.64(8)	205(8)	55231.6(1)	0.42(4)	0.0011(4)	0.17	12.98
325649	0.4836958(3)	11.0(9)	924(10)	0.3(1)	11(11)	54545.35(6)	0.73(6)	0.06(2)	0.78	130.24
289148	0.5670889(6)	—	8259(350)	0.50(3)	56(3)	53945.4(9)	2.0(3)	0.015(8)	0.45	91.59
238768	0.30033613(3)	—	2711(27)	0.99(1)	172(4)	54001.81(6)	1.7(9)	0.08(14)	0.89	116.48
265355	0.3747563(8)	10(1)	2637(700)	0.6(2)	252(19)	55911.1(4)	0.36(9)	0.0009(8)	0.16	47.26
367659	0.3096533(2)	—	8107(1308)	0.67(5)	329(10)	56234.8(2)	1.6(2)	0.008(4)	0.35	127.32
117331	0.4156716(4)	—	5959(672)	0.2(1)	169(47)	54583.2(8)	0.9(2)	0.003(2)	0.24	920.65
222500	0.3150402(2)	—	3296(589)	0.2(2)	301(62)	56634.9(3)	0.3(1)	0.0004(4)	0.12	4.36
137966	0.4018154(3)	—	3461(425)	0.2(2)	207(141)	55968.0(6)	0.4(1)	0.0010(8)	0.16	4.33
59639	1.1599840(3)	—	3842(151)	0.06(6)	233(85)	54913.9(8)	0.65(3)	0.0025(4)	0.23	19.08
40690	0.4916289(5)	—	4568(616)	0.2(1)	247(57)	54707.4(7)	0.9(2)	0.005(3)	0.31	0.3
129541	0.5992140(4)	—	5593(1810)	0.44(10)	216(24)	56753.8(5)	0.5(2)	0.0004(6)	0.12	273.27



Table 2 – continued

No.	$P_1$	$\Delta P_1$ $10^{-10}$	$P_2$	$e_2$	$\omega_2$	$\tau_2$	$a_{AB} \sin i_2$	$f(m_C)$	$(m_C)_{\min}$	$\Delta BIC$
	(d)	$\times (\text{d cycle}^{-1})$	(d)		(deg)	(MJD)	au		$M_{\odot}$	
120170	0.42183406(7)	–	2968(462)	0.5(4)	280(55)	55105.8(3)	0.17(4)	0.00007(6)	0.068	28.44
296972	0.34078361(3)	–4.38(5)	1312(1)	0.038(7)	0.3(4)	54144.096(6)	1.247(4)	0.150(2)	1.14	3631.27
146665	0.31797683(10)	–	4157(67)	0.007(10)	136(45)	57806.7(1)	2.95(6)	0.20(1)	1.29	576.0
218937	0.4387632(2)	–5.1(4)	1026(5)	0.03(3)	355(4)	53835.0(8)	0.76(2)	0.055(5)	0.75	368.45
249394*	0.44615900(2)	–	2310(4)	0.98(1)	151(9)	53825(1)	1.8(6)	0.2(2)	1.14	1720.68

Note: \* with additional periodic signal.

**Table 3.** Orbital elements from the LTTE solutions for 26 EBs in the GB10-1 field. Note that  $P_1$  is the period of the inner binary determined by the conditional entropy method plus the correction,  $c_1$ , given by the best fit of equation (2) to the ETV curve, and  $\Delta P_1 = 2c_2$ , where  $c_2$  is the second-order coefficient in equation (2), is the change in inner binary orbital period per orbital cycle in units of [day cycle $^{-1}$ ] and  $m_{AB}$  was taken as  $2 M_{\odot}$  when calculating  $(m_C)_{\min}$ .

No.	$P_1$	$\Delta P_1$ $10^{-10}$	$P_2$	$e_2$	$\omega_2$	$\tau_2$	$a_{AB} \sin i_2$	$f(m_C)$	$(m_C)_{\min}$	$\Delta BIC$
	(d)	$\times (\text{d cycle}^{-1})$	(d)		(deg)	(MJD)	au		$M_{\odot}$	
136114	0.43213930(7)	–	10211(767)	0.73(3)	255(5)	55357.7(1)	0.80(4)	0.0007(1)	0.14	105.99
64799	0.29455691(1)	–	2272(9)	0.35(2)	266(4)	54645.16(3)	0.724(8)	0.0098(3)	0.38	720.01
33369	0.234584737(3)	–	1565(12)	0.55(7)	159(5)	54014.0(2)	0.077(5)	0.000025(5)	0.047	28.18
73826	0.365257839(5)	–	1982(17)	0.39(5)	108(10)	53915.6(5)	0.088(3)	0.000023(2)	0.046	75.2
124700	0.29947914(3)	–0.72(5)	1319(4)	0.96(4)	29(10)	54272.92(2)	0.4(2)	0.006(7)	0.32	105.24
94453	0.3549125(4)	3.8(8)	5528(674)	0.41(7)	335(18)	56547.4(2)	0.6(1)	0.0010(7)	0.17	7.44
129173	0.560314938(4)	–	247.10(6)	0.04(1)	192(1)	54070.025(3)	0.296(1)	0.0566(8)	0.75	569.8
106715	0.4316864(1)	–	4375(415)	0.24(4)	249(18)	54865.5(1)	0.54(5)	0.0011(4)	0.17	162.17
15762	0.5102986(4)	–6.0(4)	3421(298)	0.61(3)	349(1)	55356.9(1)	1.7(1)	0.05(2)	0.74	1422.64
101793	0.38895230(4)	2.29(6)	745(1)	0.13(2)	241(23)	54471.29(7)	0.446(5)	0.0213(7)	0.51	533.97
89558	0.40350925(9)	–	1963(67)	0.8(2)	288(25)	54798.1(1)	0.39(9)	0.002(1)	0.21	17.79
58083	0.2510848(3)	–5.0(3)	2802(111)	0.48(6)	301(8)	54569.03(9)	0.67(6)	0.005(1)	0.3	70.96
195663	0.3003945(2)	–	6545(680)	0.90(7)	204(12)	54643.1(2)	2.3(8)	0.04(4)	0.64	14.54
181626	0.37224225(6)	20.4(1)	1221(3)	0.57(3)	77(3)	54491.62(1)	0.72(1)	0.034(2)	0.61	496.58
77420	0.66270095(8)	–	1484(356)	0.6(4)	156(117)	54350(1)	0.07(4)	0.00002(4)	0.042	61.24
181398	0.4134596(2)	–	1708(130)	0.4(3)	278(58)	54639.6(4)	0.5(1)	0.004(3)	0.28	151.49
93468	0.49273427(6)	–	3202(312)	0.6(2)	285(28)	53983.6(8)	0.20(3)	0.00011(6)	0.08	38.19
41908	0.42916153(3)	–	3881(336)	0.96(4)	131(14)	55977.8(1)	0.5(1)	0.0011(9)	0.17	15.49
124463	0.8823691(2)	–	1565(40)	0.8(2)	3(4)	55293.87(5)	0.9(3)	0.03(4)	0.61	23.15
89172	0.2596522(1)	–	6644(2795)	0.7(1)	338(13)	56438.1(6)	0.6(2)	0.0006(9)	0.14	34.29
95682	0.38272308(9)	–	2242(220)	0.2(2)	276(91)	54879.1(6)	0.29(4)	0.0006(3)	0.14	27.47
63896	0.32696380(7)	11.5(1)	1370(8)	0.73(5)	170(2)	55179.94(1)	0.48(4)	0.008(2)	0.35	124.83
174776	0.4829741(8)	–	4804(489)	0.22(5)	151(11)	58491.4(1)	3.4(5)	0.2(1)	1.36	261.24
102925	0.3926504(1)	–	3480(32)	0.383(2)	242.1(7)	56860.06(1)	3.19(4)	0.36(1)	1.7	3119.59
63946*	0.41931334(2)	–	1827(51)	0.9(1)	1(2)	54515.31(10)	0.23(10)	0.0005(6)	0.13	5.76
69632*	0.4569038(2)	–	3971(241)	0.78(2)	65(4)	57200.09(8)	0.63(6)	0.0021(6)	0.22	4.19

Note: \* with additional periodic signal.

another Python module of the MCMC fitting algorithms. For consistency between the calculations of the polynomial terms of  $E$  in equation (2) for primary and secondary eclipses, we added the phase difference between the minima of primary and secondary eclipse templates to the cycles,  $E$ , of the eclipse that is located in the second half of the folded light curve. The LTTE term in equation (2) depends implicitly on  $P_2$  and  $\tau_2$  via the true anomaly,  $v_2$ , which must be calculated by solving Kepler’s equation iteratively using a numerical method. We used Halley’s method (see, e.g. Kallrath & Milone 2009) in our study. The calculation of  $v_2$  in fact caused serious speed issues in the parameter search using `pymc`. To improve the computational speed, the calculation of  $v_2$  was performed using code written in Cython instead of Python/numpy.

The Metropolis–Hastings algorithm is used in `pymc` for distribution sampling. We adopted the built-in normal distribution function in `pymc` as the likelihood function and assumed a uniform prior for

each parameter over the boundaries that we assumed to be appropriate (see Table 1). After testing the model-fitting algorithm, we realized that the likelihood function might not be able to converge, or it might converge incorrectly to a local minimum if the initial guess of the outer period value was not close to the true value. The difficulty in having a good guess of  $P_2$  occurred particularly when only the partial LTTE cycle was observed. Concerning these problems, and with usage of the New Zealand eScience Infrastructure (NeSI) high performance computing facilities, the parameter search was carried out over a set of initial values of  $P_2$  as long as we had no confident estimation of the value of  $P_2$  by eye. For an ETV curve with a potential LTTE signal of period longer than 3000 d, for example, we ran the model fitting with initial values of  $P_2$  from 2000, 3000, 4000, 5000, 6000, 7000, 8000 and 10 000 d, respectively. For convenience, the search was over  $\log(P_2)$  space instead, bounded between  $\log(P_2/2)$  and  $\log(2P_2)$ . The initial-guess

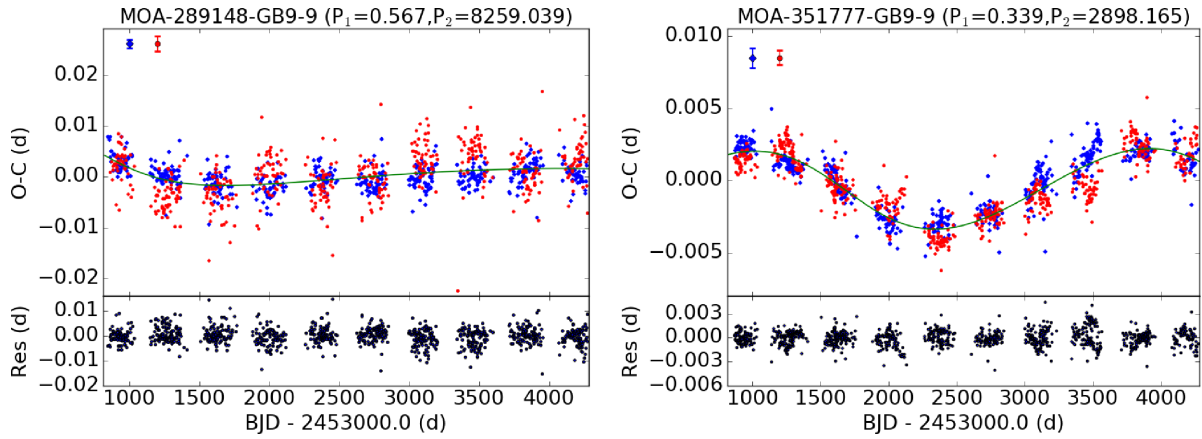


**Figure 6.** ETV curves of MOA-289148-GB9-9 and MOA-351777-GB9-9.  $P_1$  is the period of the inner binary determined by the conditional entropy method, while  $P_2$  is the period of the tertiary companion given by the LTTE solution. The blue (diamond) points are the ETV measurements of the primary eclipses and the red (circle) points are those of the secondary eclipses, while the green lines represent the best fits of the ETV model defined by equation (2). The bottom panels show the residual curves. Anti-correlated behaviours between the primary and secondary ETV curves are seen on a time-scale of a year, while the long-term trends of both curves are consistent. As can be seen in the residual curve of MOA-351777-GB9-9, for example, there is significant deviation between the trends of the primary and secondary ETV curves during the eighth MOA observational season; however, the ETV curves also exhibit consistent long-term variations. The uncertainties for the primary and secondary eclipses are represented by the red and blue error bars, respectively, at the top-left corner of each figure. Note that the periods are in days.

values of other orbital parameters, including  $e_2$ ,  $\omega_2$  and  $\tau_2$ , were taken to be the midpoints of their boundaries in principle, while the projected semi-major axis of the absolute orbit of a tertiary companion, i.e.  $a_{AB} \sin i_2$ , in au was set to be 0.5 as the initial-guess value, based on the properties of the *Kepler* triple candidates discovered by Borkovits et al. (2016), which typically have  $P_2 < 4$  yr and  $a_{AB} \sin i_2 < 1$  au.

Although mass transfer would happen in contact and semi-detached binaries, the reliability of the best-fitting solution from the LTTE model incorporating the quadratic term of  $E$  in equation (1) might be questionable, because such a combination can easily produce a satisfactory fit to a long-term ETV curve that leads to a false-positive LTTE detection. Therefore, we always preferred the best-fitting solution of the LTTE model without the quadratic term, unless the BIC value of the best fit with the quadratic term was lower than that without the quadratic term by at least 10, indicating that the best fit with the quadratic term is highly favourable. In addition, the detection of the LTTE was accepted to be genuine only if the BIC value of the best-fitting LTTE solution was lower than that of the best-fitting solution of the quadratic equation of  $E$ , which was also derived using *pymc*.

## 7 RESULTS

### 7.1 The reliability of the results

We attempted to search for LTTE in all MOA EBs of periods  $< 2$  d in the GB9-9 and GB10-1 fields. In these two fields, there are 542 EBs within the period range we were interested in. 436 and 106 of them come from the GB9-9 and GB10-1 fields, respectively.

Following the procedures of ETV analysis in the previous section, there are 91 EBs for which we could derive LTTE solutions that fit their ETV curves and, thus, we catalogized them as triple candidates. 65 of these triple candidates were identified in GB9-9, while 26 were in the GB10-1 field. The derived orbital parameters of the triple candidates are shown in Tables 2 and 3, respectively. Whether the LTTE solutions are reliable is always questionable, as several

mechanisms can produce ETV curves that mimic the LTTE. In particular, we noticed that there are a certain number of cases in which the ETVs for primary and secondary eclipses vary cyclically and behave as though anti-correlated to each other on a time-scale of a year, while the long-term trends were consistent, e.g. MOA-289148-GB9-9 and MOA-351777-GB9-9 (see Fig. 6). The anti-correlated behaviours in the ETV curves were likely attributed to star spots present on the surfaces of the EB active components (Tran et al. 2013). Generally, averaging the ETVs of the primary and secondary eclipses might reduce the contribution of such spurious ETVs. However, either the primary or secondary eclipse would usually be missing in a cycle, thus averaging was not applicable for the majority of MOA samples. Nonetheless, we recognized that the best fit obtained by *pymc* would roughly represent the solution to the mean ETV curve if we fitted the ETV curves of primary and secondary eclipses simultaneously, provided that the uncertainties in ETVs for primary and secondary eclipses are comparable.

In addition, the LTTE solution might represent the overfitting to the ETV curve when the uncertainties in the times of eclipse minima were overall larger than the LTTE amplitude. In particular, the model of quadratic ETV plus LTTE could easily provide a good fit to a ETV curve, leading to false-positive detection of LTTE. To avoid overfitting, we used the BIC to decide whether to accept or reject the solution from the model with more free parameters. In our ETV analysis, we accepted the solution of the LTTE model plus the quadratic term of  $E$  as the best-fitting one only if its BIC value was lower than that excluding the quadratic term of  $E$  by 10. Besides this, the detection of LTTE was accepted eventually only if the BIC value of the LTTE solution was lower than that of the parabolic solution. In this way, we accepted the ETV curves of 22 samples to be fitted best by the LTTE model plus the quadratic terms, while the fits by the LTTE model without the quadratic terms were preferred for 69 samples. Fig. 7 shows the plot of LTTE amplitudes,  $A_{LTTE}$ , against root-mean-square errors in eclipse timing for primary eclipses,  $\text{rms}(\sigma_p)$ . Only about half of the detected LTTE signals had amplitudes greater than the values of  $\text{rms}(\sigma_p)$ . Nonetheless, among these 91 triple candidates, 88 of them have differences between the BIC values of the LTTE and parabolic solutions larger than 10,

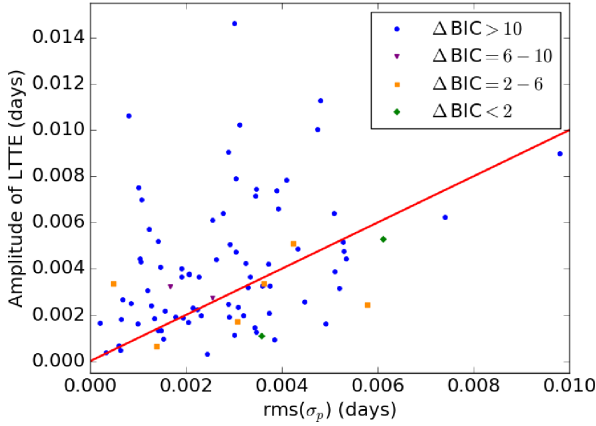


**Figure 7.** Amplitude of LTTE,  $A_{\text{LTTE}}$ , versus root-mean-square of uncertainty in eclipse timing for primary eclipses,  $\text{rms}(\sigma_p)$ , for 91 triple candidates identified in the MOA EB sample of periods  $< 2$  d from the GB9-9 and GB10-1 fields. The red line represents  $A_{\text{LTTE}}$  equal to  $\text{rms}(\sigma_p)$ . About half of these 91 triple candidates have  $A_{\text{LTTE}}$  larger than  $\text{rms}(\sigma_p)$ . The BIC was used to decide whether the ETV model with the LTTE was accepted or not. Note that  $\Delta BIC = BIC(P(E)) - BIC(P(E) + LTTE)$ , where  $P(E)$  represents the polynomial of  $E$  in equation (2) and  $E$  is the cycle. 81 of these triple candidates have  $\Delta BIC > 10$ , indicating that the best fits of the ETV model with the LTTE were strongly preferable. These 81 triple candidates include all those with inner periods  $P_1 < 0.26$  d and all those with outer eccentricities  $e_2 > 0.9$ .

indicating the LTTE solutions are very strongly preferable. On the other hand, there are two of them, MOA-40690-GB9-9 and MOA-7772-GB9-9, that have BIC differences barely above 0, indicating that the statistical evidence for detection of the LTTE in them is weak, although they are still included in the list of EBs with detected LTTE signals.

## 7.2 Statistics and distribution

Since we selected the EBs from the subfields GB9-9 and GB10-1 only in terms of period alone, this represents a homogeneous sample of EBs of periods  $< 2$  d. Therefore, it is worth examining distributions and statistics of several interesting orbital parameters.

### 7.2.1 Tertiary period

The advantage of the ETV method is that we can derive the orbital periods and eccentricities of tertiary companions from the LTTE solutions. Fig. 8 shows the distribution of the tertiary periods of all triple candidates in our sample, as well as the distributions for the triple candidates in the GB9-9 and GB10-1 fields, respectively, for comparison. We used 20 bins to bin the tertiary period from  $\log(P_2) = 0$  to  $\log(P_2) = 5$ . The tertiary period distribution peaked at  $\log(P_2 \approx 3.4)$ , which is close to the time span of the MOA data, i.e. 3420 d. Since a LTTE signal of period longer than 3420 d would only have a portion of its cycle seen in the O–C diagram, it would usually be indistinguishable from the parabolic ETV unless the portion of the LTTE curve seen in the O–C diagram has a curvature significantly different from that of a parabolic curve. Therefore, we suspect that the lack of triple candidates of longer outer period is due to the limited time span of the data. On the other side, there is almost no detection of tertiary companions of periods  $< 600$  d.

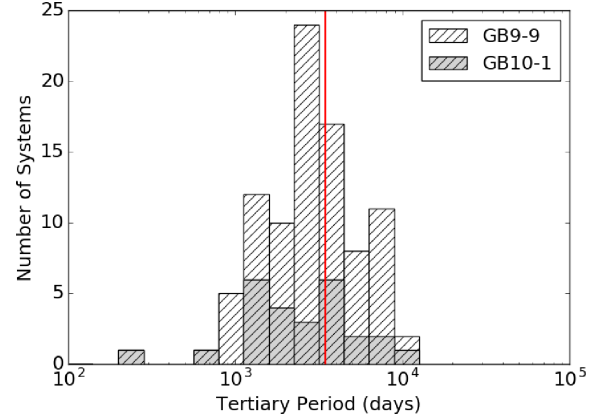


**Figure 8.** Distribution of the tertiary periods ( $P_2$ ) of 91 triple candidates identified in our MOA EB sample of periods  $< 2$  d from the GB9-9 (light) and GB10-1 (dark) fields. The distribution for the whole sample peaks at 2660 d. However, the separate distributions are not consistent with each other. The distribution for the sample from the GB9-9 field has a sharp peak at 2660 d, while the distribution for the sample from the GB10-1 field appears to be bimodal with one peak at  $P_2 \approx 3700$  d and the other at  $P_2 \approx 1300$  d. Note that the tertiary periods are binned in logarithmic bins of 20 from  $10^2$ – $10^5$  d. The red lines represent the time span of the MOA data, which is about 3420 d.

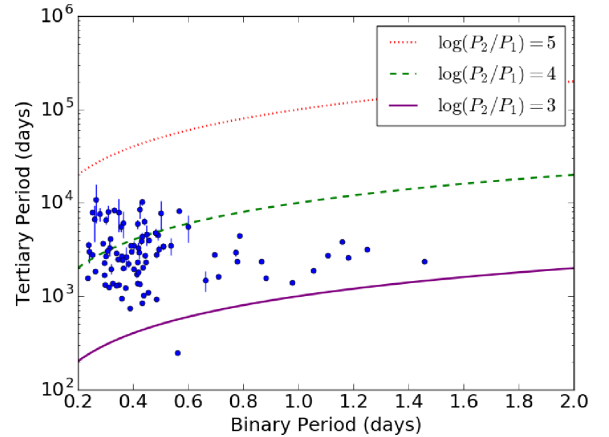


**Figure 9.** Binary period ( $P_1$ ) versus tertiary period ( $P_2$ ) for 91 triple candidates identified in the GB9-9 and GB10-1 fields. All the triple candidates have  $\log(P_2/P_1)$  between 3 and 5, except MOA-129173-GB10-1, which has a close tertiary companion of  $P_2$  about 247 d according to its best-fitting LTTE solution.

MOA-129173-GB10-1 is the only one having a tertiary companion of period shorter than 600 d.<sup>2</sup>

The lack of tertiary companions with periods  $< 600$  d might be related to the general formation process of contact binaries. However, we also have to point out that the LTTE amplitude increases as the outer period increases or the mass of the tertiary companion increases, so short-period and low-mass tertiary companions might simply be undetectable, given the uncertainties in ETV mea-

<sup>2</sup>In fact, MOA-129173-GB10-1 is one of the three triple candidates discovered in the preliminary ETV investigation of Li et al. (2017). The other two are MOA-115233-GB10-9 and MOA-360325-GB10-7 which have tertiary companions of period 427 and 482 d, respectively. However, as we are concerned with the homogeneity, we did not include these two in our sample of MOA triple candidates for statistical analysis.

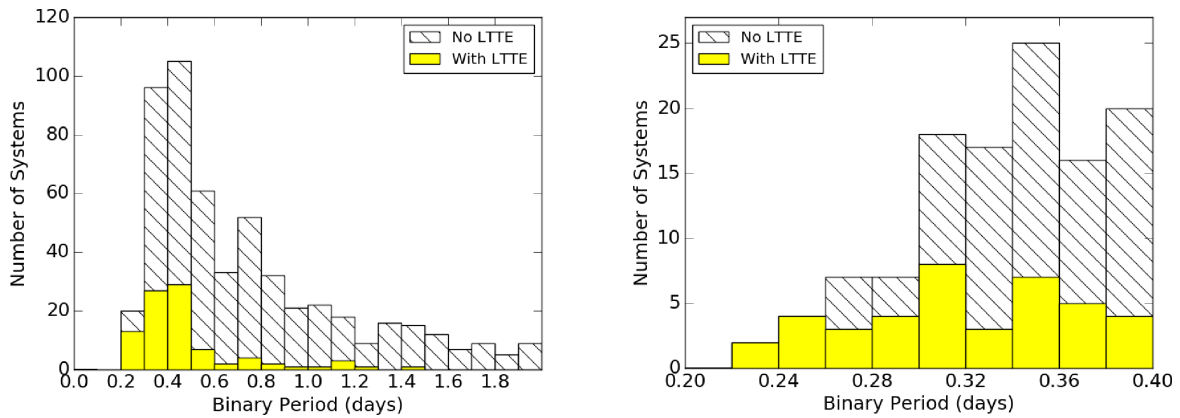


**Figure 10.** The period histogram of the 542 MOA EB sample with periods  $< 2$  d (left) and the period histogram of the subsample containing all MOA EBs with periods  $< 0.4$  d (right) from the GB9-9 and GB10-1 fields. The portion of the whole EB sample with detected LTTE signals was filled with yellow, while the rest was hatched with diagonal lines.

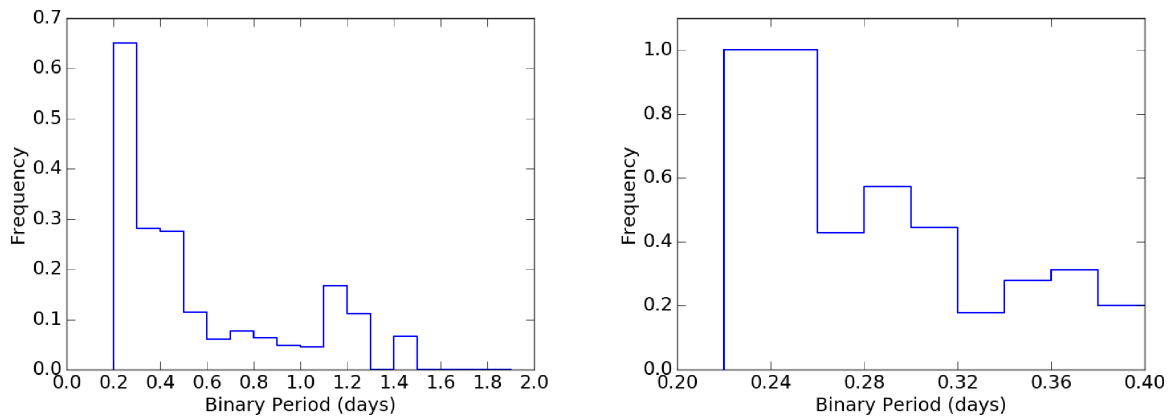


**Figure 11.** Frequency of the MOA EBs with detected LTTE signals. The frequency is defined as the number of EBs with detected LTTE signals over the total number of EBs in each bin.

measurements from the MOA data. Also, the existence of regular gaps between two MOA observational seasons in the data always results in regular gaps in the ETV curves, which in turn prevents proper coverage of short-period LTTE signals and might make short-period LTTE signals difficult to detect. In addition, the triple candidates in GB9-9 and GB9 follow distinctive outer period distributions. In particular, the tertiary period distribution of the GB10-1 sample seemed to be bimodal, with a peak at  $P_2 \approx 3700$  d and another at  $P_2 \approx 1300$  d. This could be just the effect of the small sample size, but we suspect that the peak at  $P_2 \approx 1300$  d resulted from the non-uniform density of the light curves of the GB10-1 sample, in which there are fewer data points during the first two observational seasons because lower cadences for imaging were taken towards the GB10 field during that period.

We also plotted the tertiary period ( $P_2$ ) against the inner binary period ( $P_1$ ) for the 91 triple candidates, as shown in Fig. 9. All of the triple candidates have period ratios  $P_2/P_1$  between  $10^3$  and  $10^5$ , except MOA-129173-GB10-1, for which the period ratio is below  $10^3$ .

### 7.2.2 Frequency of tertiary companions

The period distribution of our EB sample is shown in Fig. 10. The peak occurs at around 0.5 d and the number of EBs declines rapidly

when the period is longer than 0.5 d. On the other side, there is a cut-off at  $\sim 0.2$  d. The lack of contact binaries below 0.2 d in the MOA EBs is consistent with the idea of the existence of a physical lower limit of the period of contact binaries (Rucinski 1992). Looking at the period distribution of the 91 EBs with detected LTTE signals, 69 of them (i.e. 75 per cent) have periods  $< 0.5$  d, while none of them has a period longer than 1.5 d. The overall frequency of EBs with detected LTTE signals is  $91/542 = 0.168$ . If we look at the distribution of the frequency of EBs with detected LTTE signals over the period as shown in Fig. 11, it is interesting to note that the frequency basically increases as the period decreases and reaches  $13/20 = 0.65$  when the period is shorter than 0.3 d. When we further zoomed into the period range between 0.2 and 0.4 d, there are six EBs in our sample with periods shorter than 0.26 d and they all have LTTE signals detected in their O–C diagrams, giving a frequency of having tertiary companions equal to 1. Fig. 12 shows the ETV curves of these six EBs. The periods of their tertiary companions range from  $\sim 1500$  d (or 4 yr) to  $\sim 8000$  d (or 22 yr). We have to emphasize that our estimation of tertiary companion frequency is very preliminary. To obtain a robust estimation of the frequency of contact binaries with tertiary companions, corrections that take all selection effects and detection limitations into account have to be estimated through population synthesis. This would require substantial follow-up work and is outside the scope of this article.



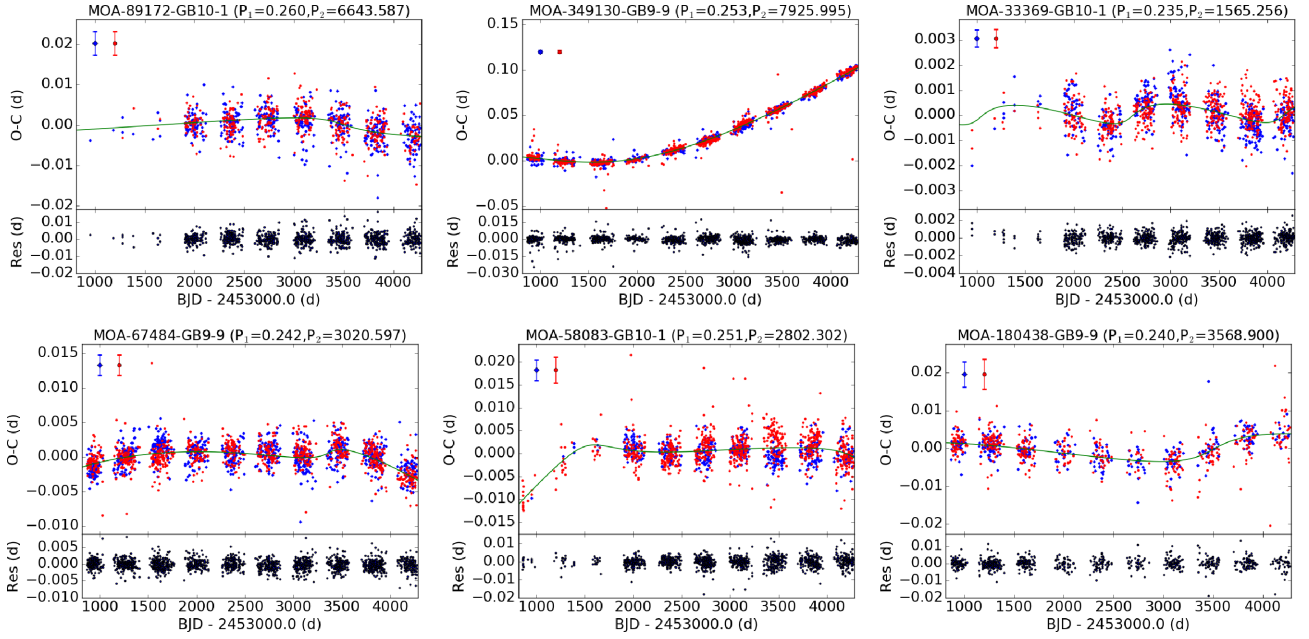


**Figure 12.** ETV curves of six EBs with periods  $< 0.26$  d.  $P_1$  is the period of the inner binary determined by the conditional entropy method, while  $P_2$  is the period of the tertiary companion given by the LTTE solution. The blue (diamond) points are the ETV measurements of the primary eclipses and the red (circle) points are those of the secondary eclipses, while the green lines represent the best fits of the ETV model defined by equation (2). Also, the average uncertainties for the primary and secondary eclipses are represented by the red and blue error bars, respectively, at the top-left corner of each figure. The bottom panels show the residual curves. Note that the periods are in days.

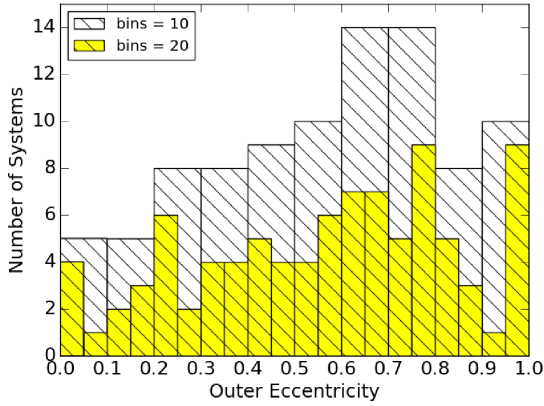


**Figure 13.** Distribution of outer eccentricity ( $e_2$ ) for 91 triple candidates in the GB9-9 and G10-1 fields. The distribution is binned into 10 (white) and 20 (yellow) bins, respectively, and they are plotted on top of each other in the same graph. The distribution increases as eccentricity increases and peaks at about  $e_2 = 0.7-0.8$ . The excess of outer eccentricity is observed at  $e_2 > 0.9$  in the triple candidates we identified.

### 7.2.3 Outer eccentricity

Another interesting property to look at is the distribution of the outer eccentricities. We plotted the outer eccentricity distributions in Fig. 13 with the number of bins 10 and 20. In the case of outer eccentricity binned into 10 bins, the distribution was characterized by a peak at  $e_2 = 0.7$ , while, interestingly, a second peak, which contains 10 triple candidates, was seen at  $e_2 > 0.9$ . When we binned the outer eccentricity into 20 bins instead, an excess was clearly noticed at  $e_2 > 0.95$ . Taking uncertainties in the eccentricity into account, the outer eccentricities of these 10 triple candidates all still fell in the range  $e_2 > 0.9$ , except for one, which just fell into the range

of  $e_2$  from 0.8–0.9. Since the excess at  $e_2 > 0.9$  is still preserved for our triple candidates when the uncertainties are concerned, such an excess is not an artefact resulting from binning.

Nonetheless, such high-eccentricity companions are expected to be so unstable that they would not survive, owing to long-term instability, or their eccentricities would not be still maintained at such large values if they formed with the inner binary systems at roughly the same time, given that contact binaries such as W UMa variables belong to old populations of ages about 4.4–4.6 Gyr (Yıldız 2014). Thus, whether the derived LTTE solutions were physical has to be examined carefully. We inspected the O–C diagrams of every EB with detected LTTE signals by eye. The LTTE solutions associated with  $e_2 > 0.9$  turned out to have unique shapes with sharp turning points (see Fig. 14), indicating the possibility of sudden changes in their orbit periods. In particular, such sudden period changes are already noticeable in the O–C diagrams of MOA-284305-GB9-9, MOA-108463-GB9-9 and MOA-249394-GB9-9. Although the values of  $\Delta BIC$  of their LTTE fits are much larger than 10, it should be emphasized that a high value of  $\Delta BIC$  simply means that the LTTE model, equation (2), which can be recognized as a mathematical model containing a combination of sinusoidal terms, gives a better description than the pure parabolic model and does not guarantee that the LTTE fit is physically reliable. Since LTTE solutions with extremely high outer eccentricities are probably unphysical, other reasons might be more appropriate to explain the observed ETVs of these 10 MOA EBs. Abrupt changes or sudden jumps in orbit periods are, in fact, not a rare phenomenon in close binaries. Dozens of close binaries, which belong to Algol or W UMa types, were reported to exhibit sudden jumps in their O–C diagrams (e.g. Narusawa, Nakamura & Yamasaki 1994; Qian, Liu & Yang 1999; Qian 2002). Mechanisms that might induce such sudden period jumps include sudden mass exchange (Helt 1987) or mass loss (Yang and Liu 2002) via stellar flares, variations in

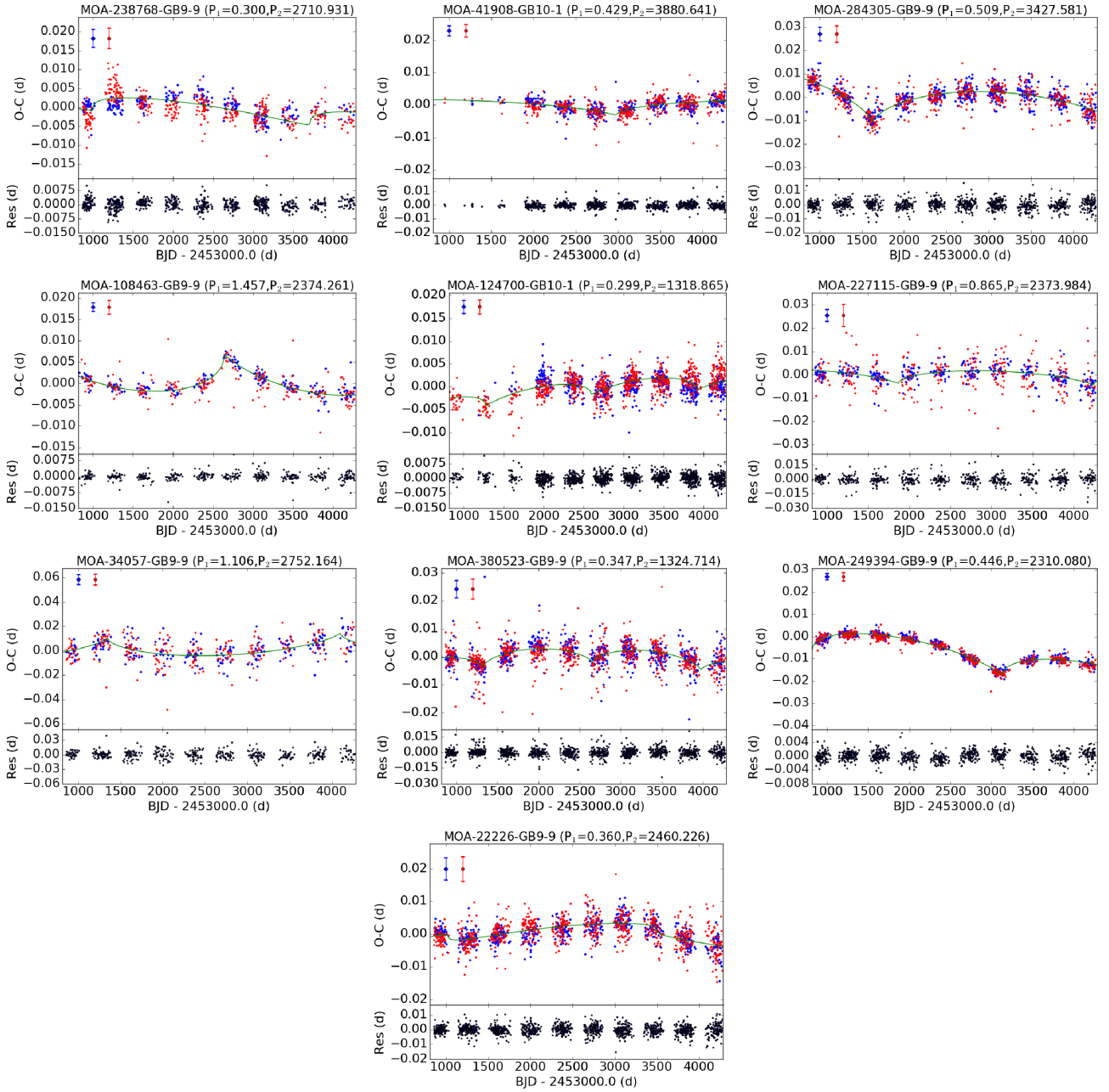


**Figure 14.** ETV curves of 10 triple candidates with outer eccentricities  $e_2 > 0.9$ .  $P_1$  is the period of the inner binary determined by the conditional entropy method, while  $P_2$  is the period of the tertiary companion given by the LTTE solution. The blue (diamond) points are the ETV measurements of the primary eclipses and the red (circle) points are those of the secondary eclipses, while the green lines represent the best fits of the ETV model defined by equation (2). Also, the average uncertainties for the primary and secondary eclipses are represented by the red and blue error bars, respectively, at the top-left corner of each figure. The bottom panels show the residual curves. Note that the periods are in days.

the internal structures (i.e. convective envelopes) of active binary components (Qian 2002) and the rapid accretion of binaries from circumstellar matter (Yang and Liu 2002). Also, the periodicity of the O–C diagrams might come from magnetic cycles arising from e.g. the Applegate effect, which can produce quasi-cyclic ETVs, instead of the LTTE from unseen tertiary companions. Despite the questionable reliability of the LTTE solutions, these 10 MOA EBs show very interesting ETVs, which are worth taking notice of.

The cumulative distribution of the outer eccentricity of the MOA triple candidates was calculated (see Fig. 15). If all 91 triple candidates are taken into account, the calculated distribution lies between

a uniform distribution and a thermal distribution.<sup>3</sup> However, as the reliability of LTTE solutions of extremely high outer eccentricities is quite questionable, inclusion of triple candidates with  $e_2 > 0.9$  might lead to an incorrect conclusion. We, therefore, excluded triple

<sup>3</sup>The term thermal eccentricity distribution refers to the distribution of eccentricities of a population of binary stars, where every member has interacted with each other and reached statistical equilibrium. The normalized distribution of such a population as a function of eccentricity is  $f(e) = 2e \, de$ , where  $e$  is eccentricity, derived by Jeans (1919).

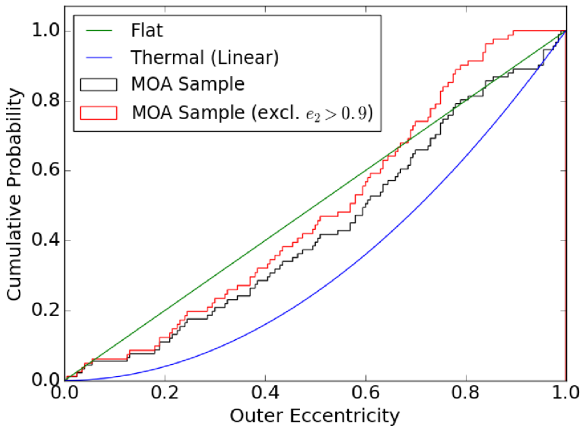


**Figure 15.** Cumulative distribution of outer eccentricity for the triple candidates identified in the GB9-9 and GB10-1 fields. The green curve represents the cumulative distribution for a uniform distribution of eccentricity from 0–1. The blue curve represents the cumulative distribution for the thermal (or linear) eccentricity distribution derived by Jeans (1919). The cumulative distributions of the outer eccentricity of the triple candidates, excluding and including triple candidates with  $e_2 > 0.9$ , in our sample are represented by the red and black curves, respectively, and their underlying distributions are distinct from each other.

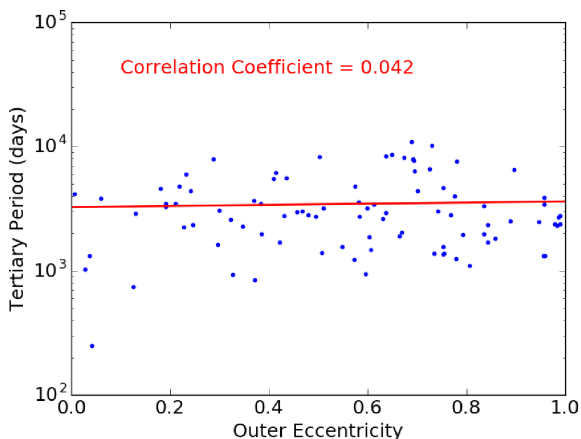


**Figure 16.** Tertiary period ( $P_2$ ) versus outer eccentricity ( $e_2$ ) for 91 triple candidates in the GB9-9 and GB10-1 fields. The red curve is the best linear fit, which has a correlation coefficient of 0.042, indicating there is no significant correlation between  $P_2$  and  $e_2$  for the group of 91 triple candidates.

candidates with  $e_2 > 0.9$  and recalculated the cumulative distribution. The recalculated cumulative distribution, in contrast to the case when all the triple candidates were included, resembles neither a linear nor a flat distribution, indicating that the issue of whether the detection of triple candidates with very high outer eccentricities was real or not could lead to very different conclusions.

The plot of outer eccentricity against tertiary period is shown in Fig. 16. The correlation coefficient was calculated to be 0.042, indicating no correlation between the outer eccentricity and tertiary period for our MOA sample.

## 8 DISCUSSION AND CONCLUSIONS

We carried out ETV analysis for a sample of MOA EBs of periods  $< 2$  d in two MOA subfields, GB9-9 and GB10-1, using MOA-II data spanning 9.5 yr. The sample contains 524 EBs, 436 and 106 in the

GB9-9 and GB10-1 fields, respectively. The Bayesian information criterion was used as a measure for model selection between ETV models with and without the LTTE term. In this way, we discovered 91 MOA EBs with detected LTTE signals, indicating the presence of tertiary orbiting companions (see Fig. 6, 12, 14, 17). The distribution of tertiary periods for our 91 triple candidates peaked sharply at 2660 d (or 7.2 yr), while there were no EBs in the sample with any tertiary companion of orbiting period  $P_2 > 30$  yr. Given the fact that the data spanned only 9.5 yr, it is obvious that the lack of detection of tertiary companions with  $P_2 > 30$  yr is a consequence of the data time span not being long enough. In addition, we suspect that the peak at 2660 d also resulted from a selection effect due to the data time span. Nonetheless, the significant decline in the distribution for  $P_2 < 10^3$  d might be related to the formation of close and contact binaries, although it might also be due to the presence of regular gaps in the ETV curves associated with the off-season periods.

As our sample was homogeneous in terms of period, it would be interesting to see how the frequency of EBs with tertiary companions varies as a function of the inner binary period  $P_1$ . In particular, the group of EBs of period  $< 0.5$  d represented a homogeneous sample of contact binaries and the detection of LTTEs in contact binaries in this period range should suffer from the lowest selection effect due to day–night cycles, as indicated by the number of eclipse time measurement points we obtained. For our sample, there is an obvious tendency for short-period contact binaries to be likely to be accompanied by tertiary companions. The frequency of our EBs with tertiary companions increases as  $P_1$  decreases. For our 13 contact binaries with  $P_1 < 0.3$  d, the frequency reaches a value of 0.65. Looking into these 13 contact binaries, we further found that all six contact binaries of  $P_1 < 0.26$  d are with tertiary binaries. Since all our detected tertiary companions have orbiting periods  $< 10^4$ , our results suggest that contact binaries with periods close to the 0.22-d contact binary limit are commonly accompanied by relatively close tertiary companions. Meanwhile, the outer eccentricity distribution for our 91 triple candidates behaved approximately as a linear function, but an excess at  $e_2 > 0.9$  was observed. In addition, long-term flux variations were seen in the light curves of most of our triple candidates. In a few cases, the flux variations are seemingly correlated with the ETVs as inspected by eye. This kind of flux variation was also observed in OGLE EBs with cyclic ETVs (Pietrukowicz et al. 2017). The long-term flux variations might come from the third light from bright stars which orbit around the EBs (e.g. Derekas et al. 2011). Nonetheless, such variations might otherwise originate from the changing luminosity of EB components associated with stellar magnetic activity or pulsations. In particular, the Applegate mechanism predicts cyclic variations in the luminosity and colours, which are correlated with orbital period variations (i.e. the O–C cycles: Applegate 1992; Lanza, Rodono & Rosner 1998; Lanza & Rodono 2002). Since there is a possibility that the detected O–C cycles for those MOA samples were driven by the Applegate mechanism, it will be necessary to examine the correlation between long-term flux variations and ETVs, in order to make better judgment on the origins of their ETVs.

In addition to the actions we mentioned in the previous paragraph, there is also much follow-up work that can be carried out in the future. First of all, given the fact that the MOA fields we investigated overlap the OGLE fields and the OGLE observations began earlier than MOA, it is worth investigating the possibility of including the OGLE data to extend the time span for ETV analysis. On the other hand, since several mechanisms such as mass transfer and the Applegate mechanism, which are often present in contact binaries, could induce long-term ETVs, the possibility of false-positive



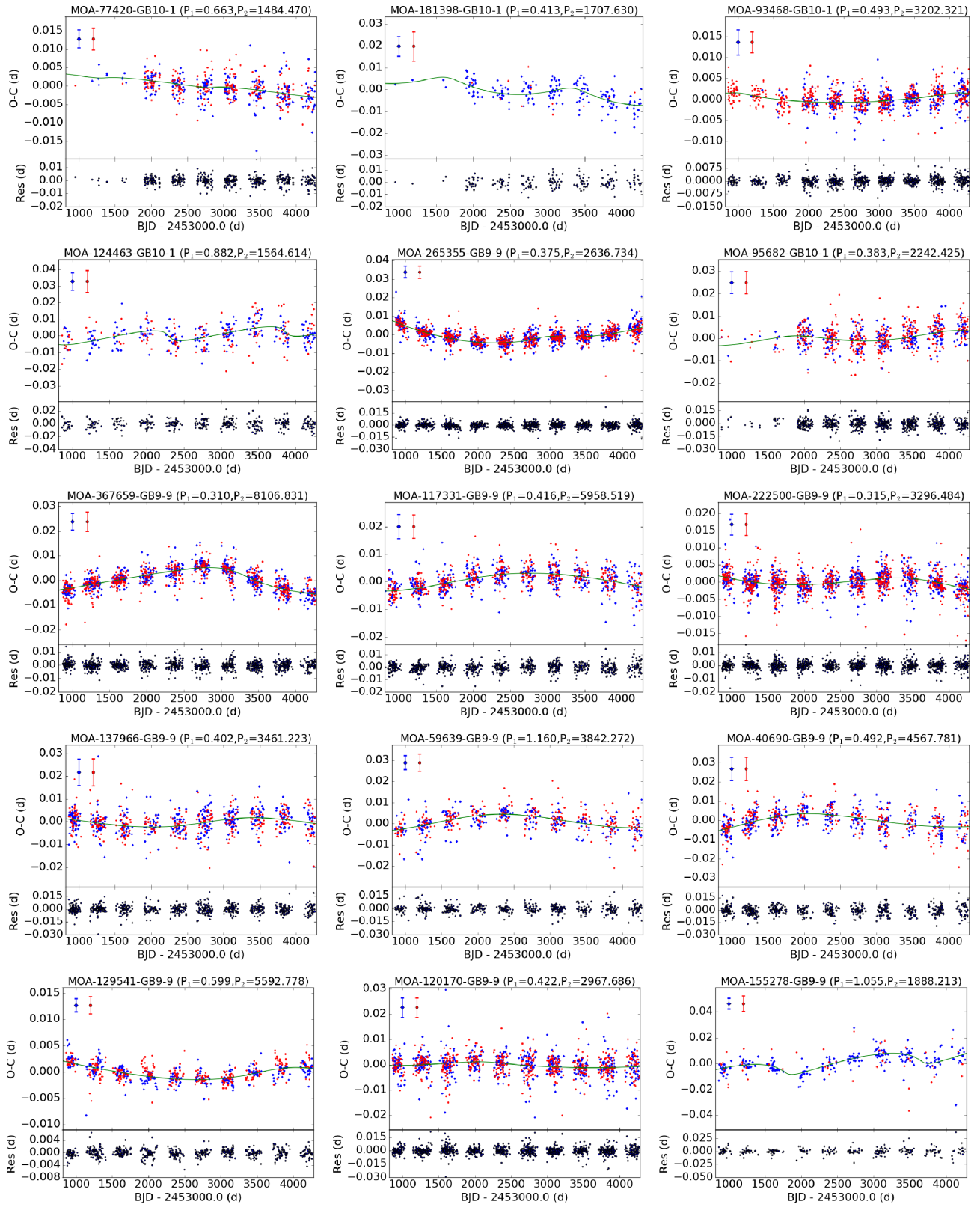


Figure 17. ETV curves of all the other 73 MOA triple candidates.



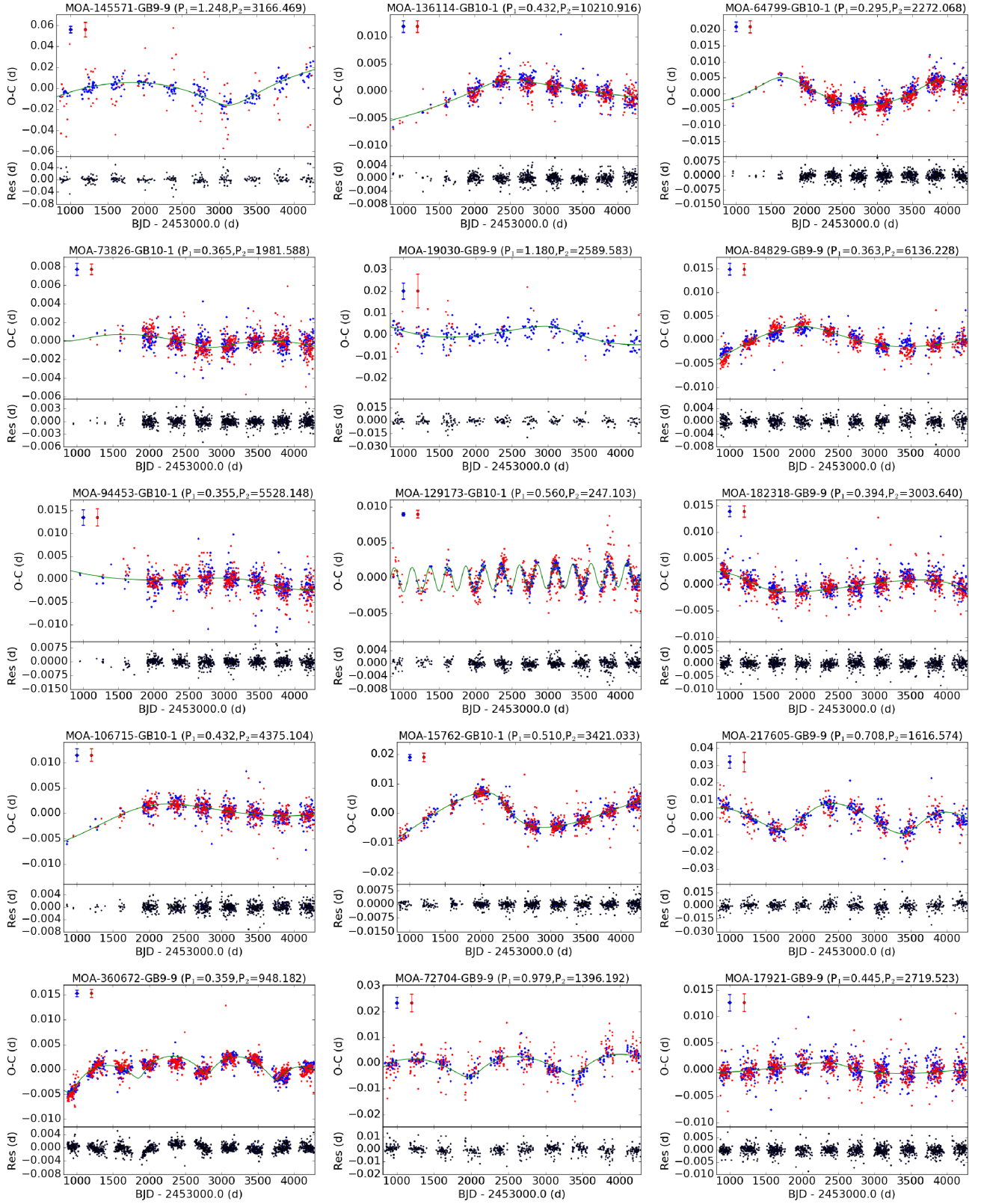


Figure 17 – continued

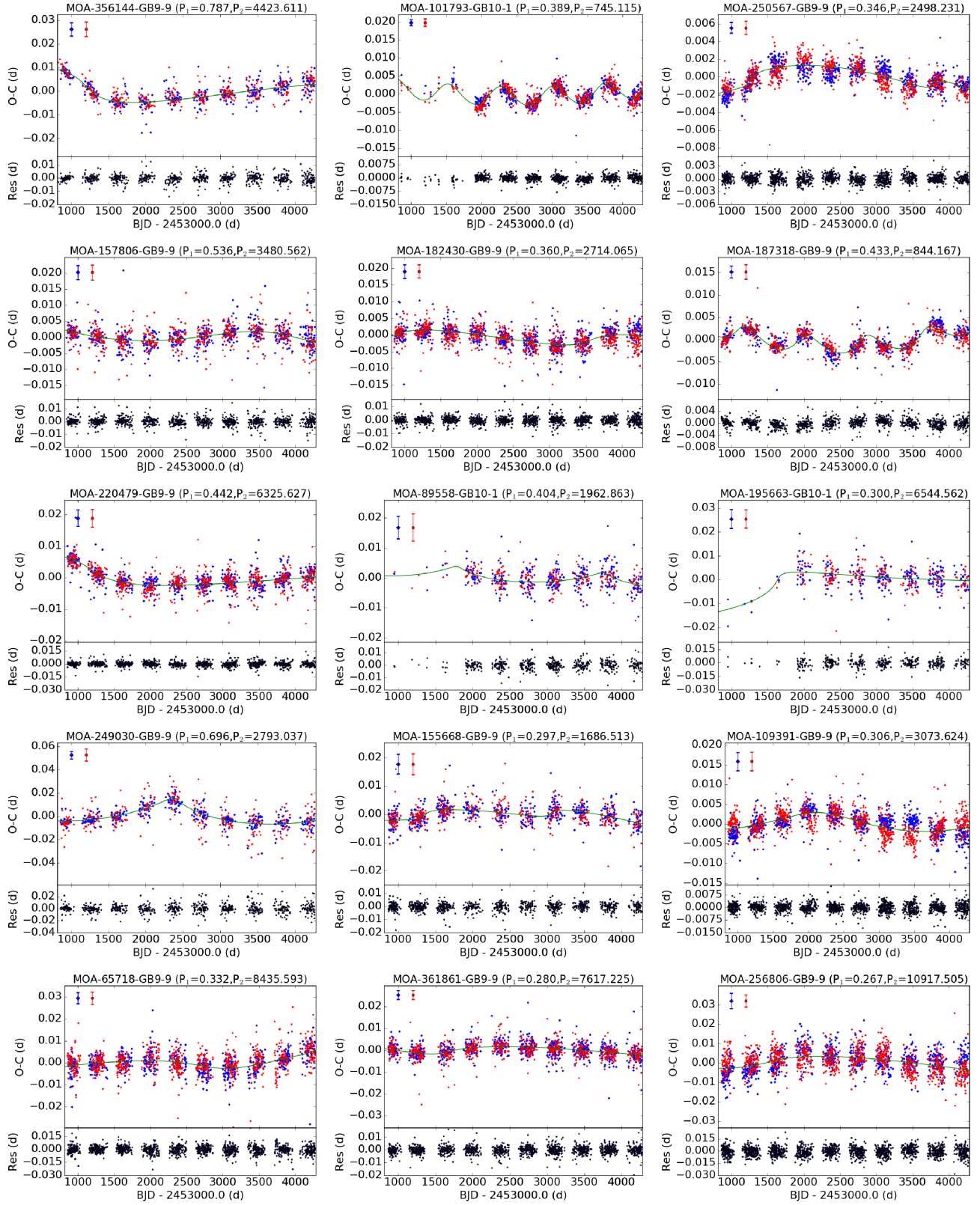


Figure 17 – continued

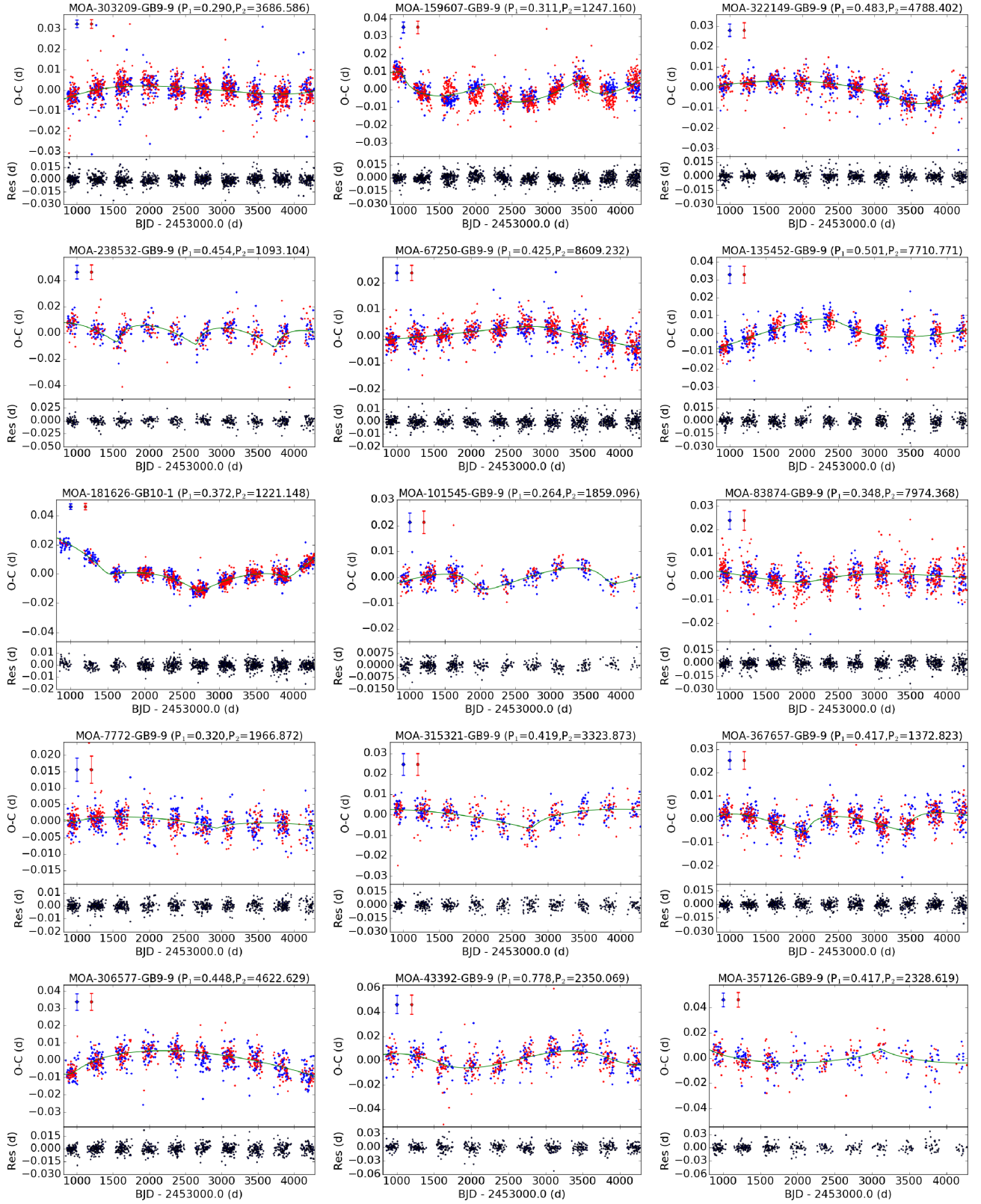
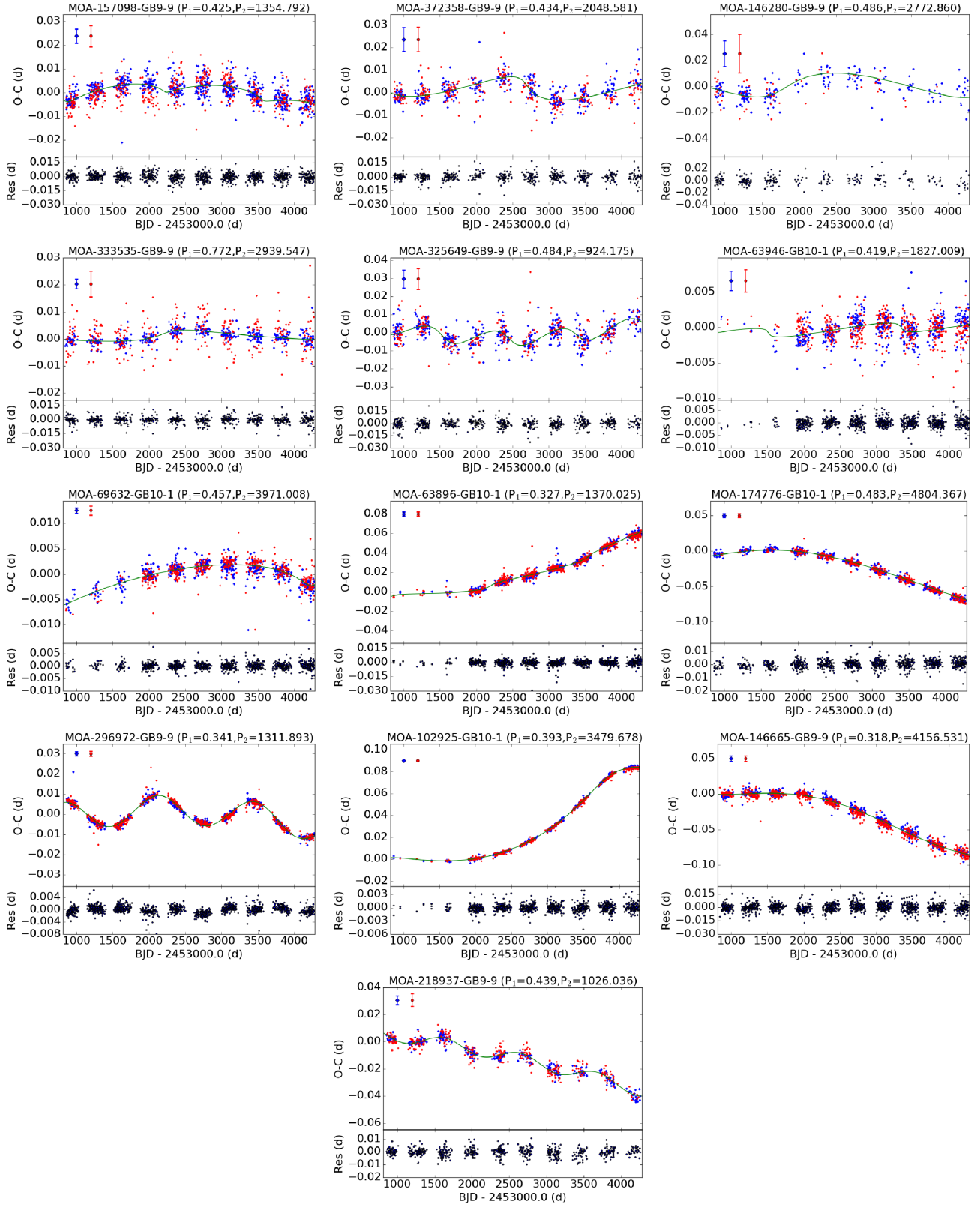


Figure 17 – continued

Figure 17 – *continued*



detection of LTTE in our sample has to be a concern. In this sense, radial velocity measurements or direct imaging would be desirable to confirm our discoveries. Also, we investigated short-period binaries only in two MOA subfields, GB9-9 and GB-10-1. We did not exploit the entire MOA EB catalogue that was established by Li et al. (2017). Therefore, the study of the multiplicity of contact binaries using a larger sample from the current MOA EB catalogue is a task that could be carried out in the near future.

## ACKNOWLEDGEMENTS

MCAL acknowledges the contribution of the New Zealand eScience Infrastructure (NeSI) high-performance computing facilities to the results of this research. New Zealand's national facilities are provided by NeSI and funded jointly by NeSI's collaborator institutions and through the Ministry of Business, Innovation & Employment's Research Infrastructure programme (<https://www.nesi.org.nz>). NJR is a Royal Society of New Zealand Rutherford Discovery Fellow. AS is a University of Auckland Doctoral Scholar. TS acknowledges financial support from the Japan Society for the Promotion of Science (JSPS) under grant numbers JSPS23103002, JSPS24253004 and JSPS26247023. NK is supported by Grant-in-Aid for JSPS Fellows. The MOA project is supported by JSPS grants JSPS25103508 and JSPS23340064 and by the Royal Society of New Zealand Marsden Grant MAU1104.

## REFERENCES

- Applegate J. H., 1992, *ApJ*, 385, 621
- Baran A. S., Zola S., Blokesz A., Østensen R. H., Silvotti R., 2015, *A&A*, 577, A146
- Barentsen G., Vink J. S., Drew J. E., Sale S. E., 2013, *MNRAS*, 429, 1981
- Bond I. A. et al., 2001, *MNRAS*, 327, 868
- Borkovits T. et al., 2014, *MNRAS*, 443, 3068
- Borkovits T., Rappaport S., Hajdu T., Sztakovics J., 2015, *MNRAS*, 448, 946
- Borkovits T., Hajdu T., Sztakovics J., Rappaport S., Levine A., Bíró I. B., Klagyivik P., 2016, *MNRAS*, 455, 4136
- Chandler S. C., 1888, *AJ*, 7, 165
- Cowling T. G., 1938, *MNRAS*, 98, 734
- Derekas A. et al., 2011, *Science*, 332, 216
- Einstein A., 1936, *Science*, 84, 506
- Foreman-Mackey D., Hogg D. W., Lang D., Goodman J., 2013, *PASP*, 125, 306
- Frieboes-Conde H., Herczeg T., 1973, *A&AS*, 12, 1
- Gies D. R., Williams S. J., Matson R. A., Guo Z., Thomas S. M., Orosz J. A., Peters G. J., 2012, *AJ*, 143, 137
- Helt B. E., 1987, *A&A*, 172, 155
- Irwin J. B., 1959, *AJ*, 64, 149
- Jeans J. H., 1919, *MNRAS*, 79, 408
- Kallrath J., Milone E. F., 2009, *Eclipsing Binary Stars: Modelling and Analysis*, Springer, New York
- Kwee K. K., van Woerden H., 1956, *Bull. Astron. Inst. Netherlands*, 12, 327
- Lanza A. F., Rodonò M., 2002, *Astron. Nachr.*, 323, 424
- Lanza A. F., Rodono M., Rosner R., 1998, *MNRAS*, 296, 893
- Lee J. W., Hinse T. C., Youn J. H., Han W., 2014, *MNRAS*, 445, 2331
- Li M. C. A. et al., 2017, *MNRAS*, 470, 539
- Mayer P., 1990, *Bull. Astron. Inst. Czech.*, 41, 231
- Mikulášek Z., 2015, *A&A*, 584, A8
- Naoz S., Farr W. M., Lithwick Y., Rasio F. A., Teyssandier J., 2013, *MNRAS*, 431, 2155
- Narusawa S. Y., Nakamura Y., Yamasaki A., 1994, *AJ*, 107, 1141
- Pietrukowicz P. et al., 2017, *Acta Astron.*, 67, 115
- Pribulla T. et al., 2012, *Astron. Nachr.*, 333, 754
- Prša A. et al., 2016, *ApJS*, 227, 29
- Qian S., 2002, *PASP*, 114, 650
- Qian S., Liu Q., Yang Y., 1999, *A&A*, 341, 799
- Rucinski S. M., 1992, *AJ*, 103, 960
- Soszyński I. et al., 2016, *Acta Astron.*, 66, 405
- Soszyński I. et al., 2017, *Acta Astron.*, 67, 297
- Sterne T. E., 1939, *MNRAS*, 99, 451
- Sumi T. et al., 2013, *ApJ*, 778, 150
- Tran K., Levine A., Rappaport S., Borkovits T., Csizmadia S., Kalomeni B., 2013, *ApJ*, 774, 81
- Woltjer J., Jr, 1922, *Bull. Astron. Inst. Netherlands*, 1, 93
- Yang Y., Liu Q., 2002, *A&A*, 390, 555
- Yıldız M., 2014, *MNRAS*, 437, 185
- Zasche P., Wolf M., Vraštil J., Pilarčík L., Juryšek J., 2016, *A&A*, 590, A85
- Zasche P., Wolf M., Vraštil J., 2017, *MNRAS*, 469, 2952

This paper has been typeset from a  $\text{\LaTeX}$  file prepared by the author.